universität wien

MASTERARBEIT / MASTER'S THESIS

Titel der Masterarbeit / Title of the Master's Thesis

„Energy transport in the atmosphere during an extreme event "

verfasst von / submitted by

Marcus Rubel, BSc

angestrebter akademischer Grad / in partial fulfilment of the requirements for the degree of

Master of Science (MSc)

Wien, 2023 / Vienna 2023

Studienkennzahl lt. Studienblatt / degree programme code as it appears on the student record sheet:	UA 066 614
Studienrichtung lt. Studienblatt / degree programme as it appears on the student record sheet:	Masterstudium Meteorology
Betreut von / Supervisor:	Univ. -Prof. Mag. Dr. Andreas Stohl

Acknowledgement

I would like to take this opportunity to thank everyone involved. First, I would like to thank Andreas Stohl and Katharina Baier, who provided me with assistance during my work and helped me, among other things, not to lose the red thread. I would also like to thank Lucie Bakels, who helped me with any difficulties I encountered in using FLEXPART. Moreover, I would also like to thank my wife, who completed her master's degree at the same time as I did, in addition to family obligations, for her additional willingness to compromise. Finally, I would also like to thank our family for their support in enabling us to complete our studies by, among other things, keeping an eye on our daughter.

Ich möchte mich an dieser Stelle bei allen Beteiligten bedanken. Zunächst möchte ich mich bei Andreas Stohl und Katharina Baier bedanken, die mir während meiner Arbeit Hilfestellungen gaben und mir unter anderem geholfen haben, den roten Faden nicht zu verlieren. Mein Dank geht auch an Lucie Bakels, die mir bei Schwierigkeiten mit FLEXPART geholfen hat. Außerdem möchte ich mich bei meiner Frau, die neben familiären Verpflichtungen zur gleichen Zeit wie ich ihr Masterstudium abgeschlossen hat, für ihre zusätzliche Kompromissbereitschaft bedanken. Schlussendlich danke ich auch für die Unterstützung unserer Familie, die es uns ermöglichten, unser Studium zu beenden, indem sie unter anderem auch ein Auge auf unsere Tochter warfen.

Table of Contents

1 Motivation

In times of climate change facts about the frequency and severity of damaging weather events are continuing to gain interest to our society. New records of precipitation amounts, damaging wind speeds and unprecedented temperatures attract strong media attention because of their destructive impacts like flashfloods, storm surges, droughts, wildfires, deaths and many more. For instance, extraordinary rainfalls caused severe damaging torrents and more than 240 fatalities in Western and Central Europe from July 12 to 18, 2021 (Cornwall, 2021). The German states North Rhine Westphalia and Rhineland-Palatinate were one of the most affected regions, where unprecedented high amounts of continuous precipitation about $150\ mm$ fell within 24 hours during the night from July 14.

Approximately two weeks before, from June 25 to 30, 2021, a “5-sigma” heat event took place over the Pacific Northwest, where previous all-time 2m-temperature records were broken by more than $5\ K$ at many weather stations (Bartusek et al., 2022). The highest temperature of $49.6°C$ was recorded in the Canadian village Lytton (50.2°N) on June 30 (UTC), which was destroyed by a wildfire because of persistent drought one day later. Without the consideration of global warming of about $1.2\ K$ this event would have been virtually impossible (Phillip et al., 2021). Even with climate change, the occurrence of such an extreme heat event is very unlikely. Figures 1 highlight the magnitude of the late June 2021 heat wave over the Pacific Northwest. Figure 1a shows the 2-m temperature over the Pacific Northwest on June 30, 2021, at 00 UTC, while figure 1b illustrates the differences between the upper outlier and the maximum of the annual maximum 2-m temperatures within the time period from 1950 to 2020 over the same region. In figure 1c the previously annual maximum 2-m temperatures’ 0^{th}, 25^{th}, 50^{th}, 75^{th} and the 100^{th} percentiles as well as the outliers over three chosen regions are shown as a box and whisker plot. The boxplots demonstrate that even the interquartile ranges (IQR) of the annual maximum temperatures are smaller than the distance between the upper outliers and the upper maximum at the end of the upper whisker. The area where the highest temperature since 1950 was exceeded by at least $6\ K$ in 2021 covers large parts of the Canadian province of British Columbia, western as well as northern parts of Alberta, and northern parts of the U.S. state of Washington (figure 1b). In a small part of western Alberta, the temperature deviated even by

more than $7.5\ K$ from the recorded absolute maximum 2-m temperature since 1950 in June 2021.

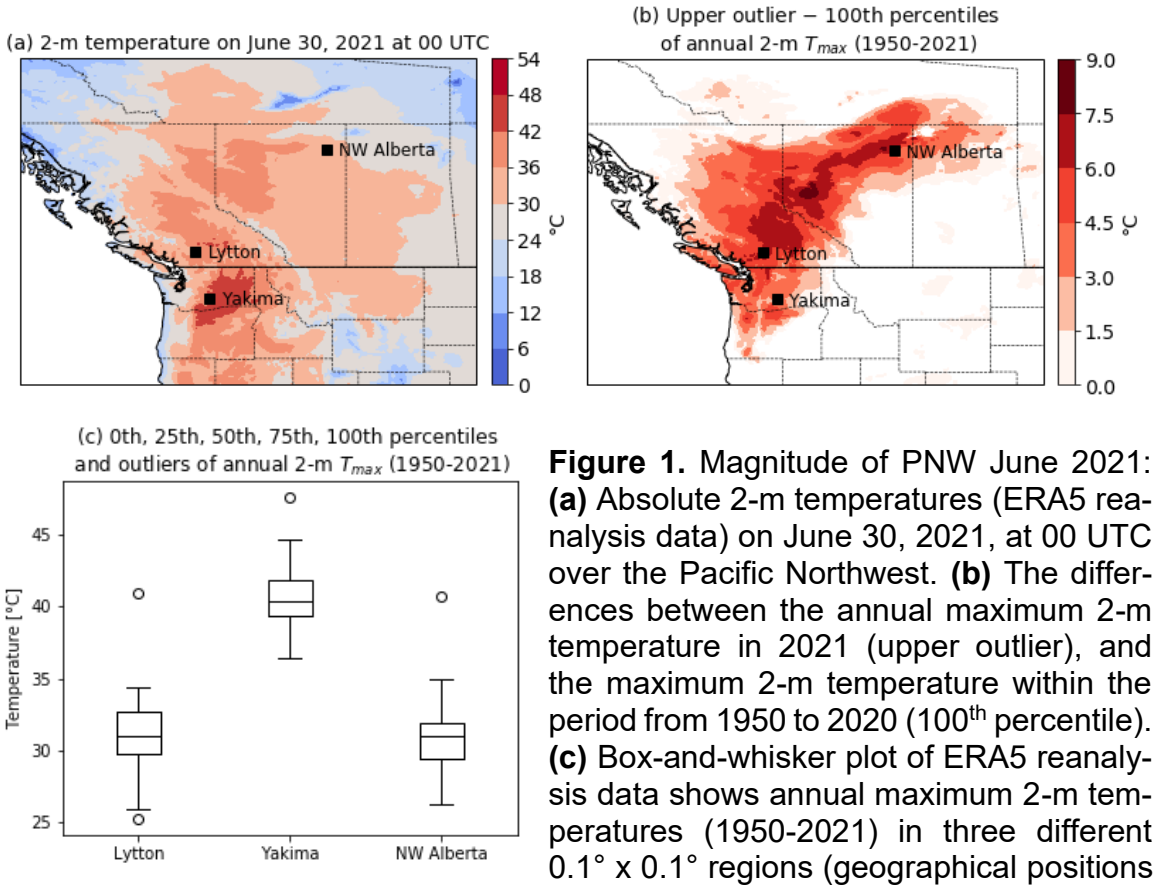

Figure 1. Magnitude of PNW June 2021: **(a)** Absolute 2-m temperatures (ERA5 reanalysis data) on June 30, 2021, at 00 UTC over the Pacific Northwest. **(b)** The differences between the annual maximum 2-m temperature in 2021 (upper outlier), and the maximum 2-m temperature within the period from 1950 to 2020 (100^{th} percentile). **(c)** Box-and-whisker plot of ERA5 reanalysis data shows annual maximum 2-m temperatures (1950-2021) in three different 0.1° x 0.1° regions (geographical positions of Lytton, Yakima and an uninhabited region around Northwest of Alberta are marked by black squares in **(a)** and **(b)**).

Bartusek (2022) stated that even events such as the June 2021 heat wave could become a decennial event over the Pacific Northwest by 2050 in case of a $2°C$ warmer climate, underscoring the importance to continue studying extreme events and their driving processes. A Lagrangian model like FLEXPART (Pisso et al., 2019) offers the opportunity to visualize energy transport and conversion of energy along trajectories. It enables scientists to reveal the driving processes and changes of meteorological parameters in a way that allows a different point of view about extreme event formations, in contrast to Eulerian data. The main question explored by the content of this master's thesis is: **Why the June 2021 heat wave over the Pacific Northwest was so anomalous in comparison to previous extreme heat events?**

2 Introduction

In the next two subsections the current state of research about the onset of heatwaves over midlatitudes and the Pacific Northwest (PNW) June 2021 event are summarized here as well as the structure and the research questions addressed. For clarity, the extreme heat event over the PNW in late June 2021 is referred to as ‘the PNW June 2021 event'. All other previous extreme heat events that occurred over the Pacific Northwest are called ‘previous PNW heat events’.

2.1 Current state of research

Usually, during a heat wave in midlatitudes, the main driving process is conversion of potential energy into internal energy by subsidence within a persistent, quasi-stationary, wave breaking, upper-level ridge during a few days until the highest temperatures occur in the affected regions (e.g., Bieli et al., 2015, Kornhuber et al., 2020). The magnitude of the heat wave depends not only on the strength of the subsidence, but also on the magnitude of any diabatic heating that occurs within ascending supersaturated air parcels preceding the subsidence. That latent heat release increases not only the potential temperature itself, but also contributes to the formation and maintenance of atmospheric blocks (Steinfeld et al., 2020). Blocking originates typically by transport of low potential vorticity along a warm conveyor belt and intrusion further downstream of it into the affected area (e.g., Zschenderlein, 2020). Other driving processes that contribute to anomalous high temperatures are warm air advection, intense insolation in accordance with clear-sky conditions and seasonality and, additionally, positive soil-moisture-temperature feedback (Oertel et al., 2023). Especially in midlatitudes where the soil moisture tends to decrease due to climate change, more energy could be available for sensible heating during future’s extreme heat events (Seneviratne, 2010).

According to various studies (e.g. Schumacher, Hauser & Seneviratne, 2022; Oertel et al., 2023), a chain of successive synoptic events led to the development of the PNW June 2021 event. Studies published shortly after the event already pointed to subseasonal variations of the East Asian monsoon system (Neal, Huang & Nakamura, 2022) or the anomalous patterns of the boreal summer intraseasonal

oscillation in Southeast Asia (Qian et al., 2022) as the origin of the PNW June 2021 event formation. A recent study, using Lagrangian methods, confirmed the origin of the air masses over the subtropical sea southeast of China (Oertel et al., 2023). Röthlisberger et al. (2023) demonstrate that during heat events near mountain ranges in the midlatitudes the dominant driver is mainly adiabatic heating. Another paper (Schumacher, Hauser & Seneviratne, 2022) pointed to one other previous heat event over the PNW for which one of the driving processes along trajectories was like the PNW June 2021 event. One of the main contributions to high near surface temperatures during heat event #13 (in Schumacher, Hauser & Seneviratne, 2022) was preceded diabatic heating due to latent heat release within ascending moist air mass. The PNW June 2021 event differs from the mentioned event #13 by diabatic heating at a considerably higher level of potential temperature. Thus, the origin of the air parcels is also essential to provide favorable conditions for the development of extreme heat events. Moreover, dry soils and low relative humidities during the PNW June 2021 event contributed to the development of a several kilometers high planetary boundary layer (PBL), in which air heats adiabatically by subsidence, entrainment and downward mixing. Thus, the daily maximum temperatures over Lytton would have been about $3 - 5\,K$ lower (Schumacher, Hauser & Seneviratne, 2022) at climatological normal soil-moisture conditions on June 28, 29 and 30, 2021.

Although a lot of important driving processes have been revealed by recent studies, some open questions remained. For instance, how the sea surface temperatures (SSTs) in the air mass source region influence the subsequent heat event and how climate change contributes to all the concatenated driving processes that occur before extreme heat events (Schumacher, Hauser & Seneviratne, 2022). Another important aspect that should be further investigated is whether any other diabatic processes heated air mass before previous PNW heat events and at what velocity the air parcels had been transported to Lytton by the ambient flow in 2021 in comparison to previous PNW heat event. However, this thesis confirms not only the results of recent studies, but also addresses some of the unsolved research questions and those given in the next subsection.

2.2 Objectives and research questions

The main research question addressed in this thesis is why the PNW June 2021 event was so “record-smashing”. Furthermore, questions about any decisive differences of the air mass origins, driving processes, and synoptic-meteorological conditions between the PNW June 2021 event and previous heat waves over the same affected area are addressed here. For instance, did the latent heat release along ascending trajectories, play a major role in the development of extreme anomalous surface temperatures only before the occurrence of the PNW June 2021 event or also during the preceding days of other previous PNW extreme events? All mentioned recent studies confirmed diabatic heating by latent heat release as one of the main driving processes before the PNW June 2021 event. However, the question remained whether other diabatic heating processes, which increase the equivalent potential temperature, θ_e, as well, occurred before previous PNW heat events. This question is addressed in this master thesis by applying the Lagrangian energy budget equation. Other connections between the onset of the PNW June 2021 event and any Foehn effects or the role of a typhoon over the western North Pacific are investigated here as well. Finally, it is investigated how the El Niño Southern Oscillation and the Pacific Decadal Oscillation relate to the occurrence of PNW heat events. Ultimately, all results will be used to evaluate whether and to what extent climate change contributed to the PNW 2021 event and where further research is required.

This master thesis is divided into four main parts and includes theoretical backgrounds, the methodology, a case study of the PNW June 2021 event and a comparison with previous PNW heat events. All equations and quantities that are used for the Lagrangian framework in this thesis are derived starting from the enthalpy equation and described in more detail in section 3. Furthermore, all used data, models and some background information about these are given in section 4 as well as the applied methods to retrace how the results are obtained. All Lagrangian and Eulerian results of the PNW June 2021 event case study and the comparison of it to previous PNW heat events are illustrated and discussed in section 5. Finally, not only remarkable differences between the driving processes and origin of air mass are discussed and conclude in the last part of this thesis in more detail, but also some limitations and remaining questions are mentioned.

3 Enthalpy equation

The base state of the atmosphere can be described by the first order approximation of the enthalpy equation for moist air, which quantifies the energy content and any conversion of it into potential and internal energy (e.g., Holton, 2004). According to the first law of thermodynamics the differential form of the enthalpy equation, dh, is written as:

$$T\,ds + \alpha\,dp = dh(T,p,q) = c_{p,m}\,dT + L\,dq \qquad (1)$$

Although, the specific heat capacity for moist air at constant pressure $c_{p,m}(p,q,T)$ and the latent heat of vaporization $L(p,q,T)$ vary slightly with pressure p, mixing ratio q and temperature T (Bolton, 1980), the latent heat of vaporization used here are given at $T = 0°C$ and $p = 1{,}000\ hPa$ by $L\ (=\ 2{,}500{,}900\ J\ kg^{-1})$ (Siebesma et al., 2020). However, slightly different values have also been reported. The specific heat capacity of moist air, that only considers liquid water here is given by the specific moisture, q, and can be written as the sum of the specific heat capacity of dry air, $c_{p,d}$, and water vapor, $c_v = c_l - c_{p,d}$, like given as follows:

$$c_{p,m} = c_{p,d} + (c_l - c_{p,d}) \cdot q \qquad (2)$$

The specific heat capacity of dry air is given at $T = 0°C$ and $p = 1{,}000\ hPa$ by $c_{p,d}(= 1{,}005\ J\ K^{-1}\ kg^{-1})$ and of liquid water by $c_l(= 4{,}219\ J\ K^{-1}\ kg^{-1})$. For simplicity $c_{p,m}$ and L are assumed to be constant in the derivations further on, where $c_{p,m}$ is replaced by c_p. The considered physical quantities in this master thesis can be derived starting from equation (1) and include a definition of the equivalent potential temperature θ_e and the Lagrangian energy equation, further on.

3.1 Equivalent potential temperature

Reordering equation (1) by the differential of the specific entropy ds lead to an expression like:

$$ds = c_p \frac{dT}{T} - \frac{\alpha}{T} dp + \frac{L}{T} dq \tag{3}$$

Equation (3) can also be stated as follows using an approximated definition of the potential temperature $\theta = T \cdot p_0^{\kappa} \cdot p^{-\kappa}$ of dry air:

$$ds = c_p \frac{d\theta}{\theta} + \frac{L}{T} dq \tag{4}$$

Neglecting variation of moisture within an air parcel can introduce errors of about $0.2\ K$ to the potential temperature (Bolton, 1980). The adiabatic exponent, κ, is the ratio between the gas constant of dry air, $R(= 287\ J\ K^{-1}\ kg^{-1})$, and c_p. Extending the last term on the right-hand side of equation (4) by c_p, pulling the temperature into the differential dq as an approximate way and integrating the equation enables to define the equivalent potential temperature, θ_e, as follows:

$$\theta_e = \theta \cdot exp\left(\frac{L \cdot q}{c_p \cdot T}\right) \tag{5}$$

with this equation 4 can be written as the following:

$$ds = c_p \frac{d\theta}{\theta} + \frac{L}{T} dq = c_p \frac{d\theta_e}{\theta_e} \tag{6}$$

The equivalent potential temperature θ_e is that temperature which an air parcel would reach if all the moisture in it were condensed out, converted into latent heat, and the air parcel were brought to a reference pressure of $p_0 (= 1{,}000\ hPa)$. The equation (6) states that the equivalent potential temperature within a closed system remains not only constant during dry-adiabatic processes, but also is conserved during moist-adiabatic processes. For instance, it is typical of moist adiabatic ascent that the potential temperature increases during ascent while the specific humidity decreases. In practice, the invariance of the equivalent potential temperature to condensation and evaporation is advantageous for many applications in meteorology. One of these would be, for example, the identification of the region of origin, characterized by climatological properties, from where the air masses come before the occurrence of extreme events. However, it should be noted that in all previous derivations the exchange with the environment such as surface fluxes or evaporation by rain droplets falling into the air mass was excluded, which limits their applicability. Furthermore, outgoing longwave radiation decreases the temperature and thus the potential temperature as well as the equivalent potential temperature by about $1\ K$ per day in a cloud-free air mass within the free troposphere (Eckhardt & Stohl, 2003). On cloud tops the rate of cooling by radiation can be about $2\ K$ per day or greater.

Another aspect that should be considered are the errors of the approximated definition of the equivalent potential temperature in equation (5) that tends to be slightly underestimated (Bolton, 1980; David-Jones, 2009). First, small errors arise putting the temperature and the specific heat capacity into the differential dq, which neglects variations of moisture within the constants itself. Furthermore, the absolute error increases nearly exponentially with increasing pressure and wet-bulb temperature and grows to about $2\ K$ at a wet-bulb temperature of $\theta_w = 22°C$ and $p = 1{,}000hPa$ (David-Jones, 2009). Despite this fact, the definition of the equivalent potential temperature in equation (5) can still be used as a sufficient approximation along trajectories that are at sufficient height above ground and in northern latitudes, where the climatological wet-bulb temperature is low enough. To be on the safe side, optimized numerical solutions of the equivalent potential temperature are used in further course of the evaluations here. During the PNW June 2021 event large portions of air mass originated from the lower troposphere over sea

surfaces with SSTs of up to 30°C, where high wet-bulb temperatures are expected. One of the most accurate formulations for θ_e is (Bolton, 1980):

$$\theta_e = \theta_{DL}\, exp\left[\left(\frac{3.036}{T_L} - 0.00178\right) q(1 + 0.448q)\right] \qquad (7)$$

where θ_{DL} is the potential temperature at the lifted condensation level (LCL) and is given by using the vapor pressure e:

$$\theta_{DL} = T \cdot \left(\frac{p_0}{p - e}\right)^{\kappa} \left(\frac{T}{T_L}\right)^{0.28q} \qquad (8)$$

The temperature at LCL, T_L, is used in equation (7) and (8) and is calculated using the dewpoint temperature T_D as:

$$T_L = \frac{1}{\frac{1}{T_D - 56} + \frac{ln(T\,/\,T_D)}{800}} + 56 \qquad (9)$$

A comparison of several numerical solutions of the equivalent potential temperature demonstrated that the maximum absolute error of equation (7) is about $0.035\ K$ within a pressure range of $100hPa$ and $1{,}050\ hPa$ and at a wet-bulb temperature of up to $32°C$, or $\theta_e \leq 126.85°C$ (David-Jones, 2009). Equation (7) is used to calculate θ_e for all evaluations in this master thesis and can be calculated by importing the open-source python module *metpy v1.4* (for python versions 3.8 or newer).

3.2 Lagrangian thermodynamic energy equation in pressure coordinates

To investigate processes along trajectories the Lagrangian total time derivative of the temperature is used, which is divided into a Eulerian local time derivative of temperature and advection of the three-dimensional temperature gradient. The differential equation is given as follows:

$$\frac{dT}{dt} = \frac{\partial T}{\partial t} - \boldsymbol{u} \cdot \boldsymbol{\nabla T} \tag{10}$$

Next, another expression is sought that can be substituted on the right-hand side of equation (10) and includes diabatic and adiabatic processes. Reordering equation (1) by the infinitesimal temperature change, dT, dividing it by an infinitesimal time derivative, dt, and c_p yields:

$$\frac{dT}{dt} = \frac{T}{c_p}\frac{ds}{dt} - \frac{L}{c_p}\frac{dq}{dt} + \frac{\alpha}{c_p}\frac{dp}{dt} \tag{11}$$

Equation (11) can also be rewritten in terms of changes in equivalent potential temperature instead of changes in specific entropy by using equation (6) and is read as:

$$\frac{dT}{dt} = \frac{T}{\theta_e}\frac{d\theta_e}{dt} - \frac{L}{c_p}\frac{dq}{dt} + \frac{\alpha}{c_p}\frac{dp}{dt} \tag{12}$$

Furthermore, the second expression on the right-hand side of equation (12) is multiplied by T/T. The temperature in the first expression and in the numerator of the previously extended factor is replaced by the definition of the potential temperature $T = \theta \cdot p_0^{-\kappa} \cdot p^{\kappa}$. The resulting equation is given as follows:

$$\frac{dT}{dt} = \theta \left(\frac{p_0}{p}\right)^{-\kappa} \left(\frac{1}{\theta_e}\frac{d\theta_e}{dt} - \frac{L}{T}\frac{dq}{dt}\right) + \frac{\alpha}{c_p}\frac{dp}{dt} \qquad (13)$$

Inserting equation (6) into the bracket of the first term on the right-hand side in equation (13) leads to an equation that includes the heating rate $H = \frac{d\theta}{dt}$. Rewriting the second term on the right-hand side of the equation (13), using the ideal gas law for dry air, $p\alpha = RT$, the adiabatic exponent, κ, and the definition of the vertical displacement in pressure coordinates, $\omega = \frac{dp}{dt}$, the nonlinear total time derivative of the temperature can be stated as follows.

$$\frac{dT}{dt} = \left(\frac{p_0}{p}\right)^{-\kappa} H + \frac{\kappa T}{p}\omega \qquad (14)$$

According to the first term on the right-hand side of equation (12) and (13) diabatic contributions to temperature changes along trajectories occur through changes of moisture and changes of θ_e. The specific humidity, q, can predominantly change due to surface fluxes along trajectories within the boundary layer or phase transitions, for instance contributes to diabatic heating by condensation during moist-adiabatic ascent. Another phase transition that is more difficult to deal with in the Lagrangian framework is any evaporation of precipitation falling through air mass in the free troposphere. Moreover, the temperature and thus the equivalent potential temperature are affected by the divergence of fluxes, $-\nabla \cdot F$, within an air parcel. In higher altitudes, where surface fluxes are negligible, and during clear-sky conditions outgoing longwave radiation dominates and consequently the fluxes F diverge and lead to a decrease in T and θ_e by a rate of about $1K$ per day. Adiabatic processes along trajectories are given by the second term on the right-hand side of equation (14) and driven by uplift as well as subsidence of the associated air parcel.

Depending on the expected meteorological condition at the respective trajectories' position, one or other contribution by diabatic processes can be excluded. For instance, trajectories that are above the planetary boundary layer and contain low specific moisture leading to a spread between temperature and dewpoint greater than 10 K (Chernykh, & Eskridge, 1996) leading to clear-sky conditions. In another example, particles that move in the boundary layer where moisture doesn't condense, diabatic processes occur mainly due to surface fluxes. Under certain conditions, such distinctions reveal the portions and magnitudes of each driving process that contributes to extreme anomalous temperatures. Equation 12 is utilized to confirm the hypothesis that diabatic heating had been caused mainly by latent heat release during moist-adiabatic ascent before the dry adiabatic descent started and contributed to the extreme near surface temperatures during the PNW June 2021 event. Since θ_e and its applications have been introduced, another conserved quantity can be additionally used for evaluations along trajectories further on and is briefly described in the next subsection.

3.3 Ertel potential vorticity

By combining the vector vorticity equation and thermodynamic equation one can derive (not shown here) the Ertel potential vorticity, P, in z-coordinates, which is given by (Hoskins, 1997):

$$P = \frac{1}{\rho} \cdot \boldsymbol{\zeta} \cdot \nabla\theta \qquad (15)$$

Equation (15) includes the density, ρ, the three-dimensional vector of absolute vorticity $\boldsymbol{\zeta}$ and the gradient of the potential temperature between the two isentropic surfaces in which the rotation is embedded. To investigate when P is conserved the material derivative must be applied on equation (15) which yields to an expression like:

$$\frac{DP}{Dt} = \frac{1}{\rho} \cdot \boldsymbol{\zeta} \cdot \nabla\dot{\theta} + \frac{1}{\rho}(\nabla \cdot \boldsymbol{F})\nabla\theta \qquad (16)$$

Here, the diabatic heating/cooling rate is given by $\dot{\theta} = D\theta/Dt$ and the vector of friction by $\boldsymbol{F}$. Any diabatic heating or momentum source leads to an increase in potential vorticity. The potential vorticity P is conserved if the right-hand side of equation (16) vanishes. This is the case when there is neither diabatic heating or cooling nor friction. The statement above is used to evaluate if either the processes along trajectories are adiabatic and frictionless or not.

Furthermore, the z-component of the absolute vorticity includes the relative vorticity ξ and the Coriolis parameter f. Thus, the material tendency of the potential vorticity also depends on the sign of ξ, which is positive within cyclonic and negative within anticyclonic flows. Any decreasing value of P indicates not only diabatic cooling, but also that the trajectories' shape is increasingly becoming anticyclonic. Notwithstanding, the potential vorticity is limited by the two-dimensional internal stability criterion, given as $\xi + f > 0$ (Lin, 2007), and thus cannot become negative in the northern hemisphere. The properties of the potential vorticity are used to evaluate any streamline shapes as well.

In addition, the potential vorticity can be used to define the tropopause height. For instance, Ertel (1942) defined the dynamical tropopause threshold at 2 potential vorticity units ($1\ \mathrm{pvu} = 10{-}6\ \mathrm{K\ m^2\ kg^{-1}\ s^{-1}}$), which is used to address the question whether any air descended from the tropopause or even the stratosphere during the PNW June 2021 event. However, another more recent study (Kunz et al., 2011) defined the tropopause height differently, whose thresholds are described in more detail in the case study in section 5.2.

4 Methodology

All methods that are applied in this master thesis to study extreme heat events are described in this section. The use of backward computed Lagrangian data (by FLEXPART) is a core part of this work to reveal decisive differences of energy transport and driving processes between the PNW June 2021 event and past PNW heat events. The case study of the PNW June 2021 event includes Eulerian data as well to compare them with driving processes along air parcels before, during, and shortly after the event peak. Additionally, Eulerian datasets are compared with the Lagrangian analysis data during and before the 32 most intense PNW heat events between 1960 and 2021 in section 5.5.

4.1 ERA5-reanalysis and DOISST v2.0 data

The fifth generation ECMWF (ERA5) atmospheric reanalysis data (Hersbach et al., 2020) are utilized not only as input data for the FLEXPART model, but also as Eulerian data to visualize the synoptic situation first. This thesis includes reanalysis data of θ_e and the geopotential height on different pressure levels as well as ERA5-Land reanalysis data of 2-m temperature, specific humidity and skin reservoir content to represent the meteorological situation during and before the PNW June 2021 event.

The model that computes ERA5 reanalysis data has been developed to replace the ERA-Interim reanalysis data, among others, and is based on the Integrated Forecast System (IFS) Cy41r2. The recent update of IFS was operational in the ECMWF medium-range forecasting system from 2016 and benefits from decades of research, which has improved core dynamics and model physics. For instance, the radiation scheme, the large-scale cloud and precipitation scheme and orographic drag are relevant model physics used for the Eulerian as well as for the Lagrangian investigations in this thesis. Moreover, the improvements in soil evaporation schemes concern evaluations of any soil-moisture-temperature feedback. In addition, not only the model physics had been improved in ERA5 compared to its predecessor ERA-Interim reanalysis data, but also the data assimilation methods and its components. ERA5 analysis data have been computed using the Four-

Dimensional Variational data assimilation (4D-Var). Notably, ERA5 also has increased spatial and temporal resolution output. The global ERA5 data have a temporal resolution of 1 hour at a grid size of about 0.5° x 0.5° over 137 vertical levels.

Moreover, the estimate of the background error covariance matrix using 10 members in the ensemble data assimilation scheme (EDA) is a new component in ERA5. Their data qualities are estimated by the ensemble spread and varies with height and meteorological parameter like temperature, pressure, wind field or specific humidity (e.g., Figure 12 in Hersbach, 2020). The uncertainty of temperature varies from about $0.4\,K$ to $0.6\,K$ in the 1980s and from $0.2\,K$ to $0.4\,K$ in the 2010s. Furthermore, the uncertainties of ERA5 wind field data used for FLEXPART ranges from about $0.5\,m\,s^{-1}$ at $1{,}000\,hPa$ to $1.5\,m\,s^{-1}$ at $300\,hPa$, depending on the considered time period as well. The specific moisture exhibits the greatest uncertainty in the middle and upper troposphere and ranges from about $3-4\,\%$ in $1{,}000\,hPa$, $7-10\,\%$ in $850\,hPa$ to up to $20\,\%$ in $500\,hPa$ within a time period from 1980 to 2020 and further affects the uncertainty of the equivalent potential temperature $\theta_e\big(q,T,\theta(p,T)\big)$. Therefore, subsequent errors should be considered when illustrating θ_e, which represents the energy content in the atmosphere. The temporal decline of ensemble spread of all quantities can be explained by the increase in availability of observations and the higher accuracy of the measurement instruments. For instance, the number of daily assimilated observations doubled about five times within a time period of 40 years and was about 24 million per day in 2019. Various In-situ measurements, for instance, land and ship stations, drifting and moored buoys, radiosondes and dropsondes, aircraft-based observation, are used in the 4D-Var assimilation. In addition, further information from remote sensing instruments such as from over 200 satellites or radars are utilized to support the accuracy of analysis data obtained from 4D-Var, especially in higher levels of the atmosphere, where a large portion of investigated air mass are expected to be in the Lagrangian framework of this thesis.

In order to evaluate and compare the SSTs around the origin regions of air parcels before the individual heat wave, DOISST (Daily Optimum Interpolation Sea Surface Temperature) v2.1 data (Huang et al., 2021), provided by NOAA (National Oceanic and Atmosphere Administration) are used. The DOISST v2.1 data has a spatial

resolution of 0.25° x 0.25°, a temporal resolution of 24 hours and is obtained by combining two different types of SST products. The first product includes Argo in-situ measurements from ships and different types of buoys whereas SST data provided by the second type of product is retrieved purely from satellite data. The global mean root-mean-square differences of SST between the two products is $0.38\ K$ and its mean over the western Pacific Ocean is about $0.2\ K$.

4.2 ERA5 data over mountainous terrains

Lytton's ERA5 2-m temperatures deviate by about $9\ K$ from the weather station measurement there ($41.2°C$ vs. $49.6°C$ on June 30, 2021) due to differences between the real and model topography in the mountainous environment (peaks are over $2{,}000\ m$). The calculation method of gridded ERA5-Land data of 2-m temperature is implemented by interpolations between the lowest model level and the Earth's surface (Muñoz-Sabater, 2019). The native resolution of hourly ERA5-Land data is about 9 km and cannot fully resolve the narrower Lytton valley (195m asl.) accurately enough to interpolate temperatures below about $1{,}000\ m$ there. Under the assumption of a dry adiabatic temperature lapse rate during heat events this circumstance results in a deviation of about $8 - 9\ K$ between ERA5-data and the weather stations around Lytton. Nevertheless, showing temperature differences with ERA5-Land data like in figure 1 above are still justified because the mentioned computation methods are valid equally for all available dates.

4.3 FLEXPART Model

The FLEXPART model (Pisso et al., 2019) is used in this thesis to obtain Lagrangian analysis data of each considered extreme heat event. FLEXPART was developed in 1998 by a few scientists to calculate the long-range and mesoscale dispersion of pollutants, which are transported by atmospheric flows to better predict, for instance, the impacts of a nuclear power plant accident (Stohl et al., 2005). FLEXPART is a stochastic model that transforms Eulerian input data into Lagrangian trajectories and has the option to run forward or backward in time.

Compared to Eulerian models, FLEXPART has the advantage that Lagrangian trajectories can be more easily traced back due to their independence of a computational grid. Consequently, the numerical discretization of stochastic differential equations causes smaller numerical errors in Lagrangian models (Ramli & Esler, 2016), than those which occur in tracer transport with Eulerian or semi-Lagrangian models (Cassiani et al., 2016). The ability to simulate fine tracer structures created by transport allows resolving energy transport in filamentary structures such as a warm conveyor belt (Stohl et al., 2003) and their contributions to the development of extreme high near surface temperatures farther downstream more accurately than Eulerian models, which have difficulties to resolve the mentioned structures (Rastigejev et al., 2010). All used input data and other settings of FLEXPART for further investigations are described in the next subsection in more detail.

4.4 Lagrangian analysis data of PNW heat events

For the analysis, FLEXPART was run with hourly $0.5° \, x \, 0.5°$ ERA5 data as input. 10,000 particles were released and traced 15 days backward in time. This is done for all extreme heat events detected over the Pacific Northwest (see section 5.5). The geographical position of the trajectory release box, which had an area width of 1° x 1°, is centered over Lytton (50.2°N, 121.6°W) during each PNW heat event and ranges from 10 m to 3,000 m above ground level, thus, 2,500 particles started from each considered 0.5° x 0.5° grid cell. The release date of each PNW event including the PNW June 2021 event is when the highest 2-m temperatures were recorded during the respective heat event peak. The trajectories' starting time for all simulations is simultaneously at 00 UTC (5 pm local time) and corresponds roughly to the daytime when highest daily 2-m temperatures occur. For the PNW June 2021 event additional 3 simulations over 2 days (June 28 – June 29, 2021) before and one day (July 1, 2021) after the event peak are done. Following variables are stored as hourly data: three-dimensional geographical trajectory positions and wind components, temperature, specific humidity, potential vorticity, density, particle mass and mixing height.

In addition, some differences between the trajectory models and configurations applied here and in two others recent Lagrangian studies about the PNW June

2021 event should be mentioned. The most important difference between FLEXPART, TRACMASS (Döös, Jönsson & Kjellsson, 2017) and LAGRANTO 2.0 (Sprenger and Wernli, 2015) is the convection and turbulence parametrization scheme are only included in FLEXPART (Pisso et al., 2019). Furthermore, Röthlisberger and Papritz (2023) investigated not only the PNW June 2021 event, but also worldwide heat waves by using 15-day backward trajectories as well. Due to the release of about 250,000,000 particles over the entire globe and considered time period, much fewer particles were started from each 0.5° x 0.5° grid cell and respective heat event (24 particles). Moreover, the data are stored at lower temporal resolution (3 hours). Another Lagrangian study about the PNW June 2021 event (Schumacher, Hauser & Seneviratne, 2022) used higher resolved ERA5 data (hourly, 0.25° x 0.25°) as an input than in this thesis. Additionally, they demonstrated that changes in temporal and spatial resolution of ERA5 reanalysis data causes only minor differences in Lagrangian output data, thus, no major deviations from the results in Schumacher, Hauser & Seneviratne (2022) and Röthlisberger & Papritz (2023) are expected to occur in this thesis by using hourly 0.5° x 0.5° ERA5 data. Moreover, the number of released particles within each 0.5° x 0.5° grid cell was less as well (about 688 particles) in Schumacher, Hauser & Seneviratne (2022). Since both studies revealed similar results with respect to the driving processes during the PNW June 2021 event, although they released on order of magnitude different numbers of particles, no significant differences are expected to occur in this by releasing 2,500 particles per 0.5° x 0.5° grid cell in the end.

4.5 Identifying extreme heat events in the Pacific Northwest

In order to identify extreme heat events a percentile-based filtering method was used for the area over Lytton. For statistical significance, at least 30 extreme heat events must be investigated and were identified for the period from 1960 to 2021. First, the overall warming trend contained in the daily maximum 2m-temperatures from 1960 to 2021 were removed to obtain heat events that are as uniformly distributed as possible over the considered period. Without detrending the data, most of the 30 detected heat events would have accumulated within the last two decades.

In a next step, I defined the self-chosen 99th -percentile threshold of the daily maximum 2-m temperatures. Within a time period of 62 years (1960 – 2021), the daily maximum 2-m temperature can only be above this threshold for a maximum of 226 days. Previous studies that investigated hot and cold extreme events used a higher threshold of 99.5th or 99.9th -percentile because they used a larger 6-hourly dataset instead of daily data that contains less entries (e.g., Bieli et al., 2015). Each heat event is identified according to two criteria. On the one hand, the temperature should be over the 99th -percentile on at least two consecutive days, on the other hand, the period between each temporary temperature peak should be at least 7 days to classify approximately the event as an individual one. Moreover, another study that investigated the PNW June 2021 event and previous ones used annual daily maximum temperatures and temperatures above the 3-sigma threshold around the PNW regions as a guideline to identify previous events (e.g., Röthlisberger & Papritz, 2023). One difference between using the 3-sigma threshold and the percentile-based method, used in this thesis, is that heat waves are considered at the same location instead of different ones. Another caveat occurs between the usage of the 99th – percentile threshold and the of annual maximum temperatures itself. About the lowest quarter of the annual maximum 2-m temperatures around Lytton within 1960 and 2021 are well below the 99th – percentile threshold, even below the 95th -percentile in some years, as it can be demonstrated with ERA5-Land reanalysis data. For this reason, the percentile-based method is preferred here. The date, duration and other information such as the Niño 3.4 and Pacific Decadal Oscillation indices of each PNW heat event are listed in table 1 (see subsection 6.2).

4.6 Revelation of driving processes applying the Lagrangian energy equation

All adiabatic and diabatic processes are subdivided based on equation (12) and (13) into processes like vertical displacement, changes of θ_e and specific moisture. In contrast to the paper published by Röthlisberger (2022), I used the thermodynamic energy equation in this thesis to examine individual driving processes that led to the extreme near surface temperatures instead of the Lagrangian

temperature-anomaly equation. Starting from particles within the lowest $150\,m$ above ground, the absolute changes of *p, q* and θ_e, are computed along the trajectories from backward day 10 as well as day 5 to the respective PNW event's peak. Selecting trajectories within the lowest $150\,m$ out of a $3{,}000\,m$ high release box reduces the number of particles from $10{,}000$ to about 500 for each event.

To replace all quantities (α, T and p) that are assumed to be constant and are beyond the differentials in equation (12) the mean value of them at the edges of the respective time period are calculated. For instance, $\frac{T(-10d)+T(0d)}{2}$ is inserted in the first term on the right-hand side of equation (12). Furthermore, the trajectories' mean changes of pressure, specific moisture and θ_e that contributed to ΔT are compared together and finally added up starting from the trajectories' mean temperature 10 days and 5 days prior of each PNW event. For verification, I compared the particles' mean total temperature change obtained by the energy equation, ΔT_{EE}, with those computed by the computed Lagrangian FLEXPART data ΔT_{FP}. The calculation errors that arise from the application of the Lagrangian energy equation are estimated by the ratio of ΔT_{EE} and ΔT_{FP}, which is written as:

$$\frac{\Delta T_{EE}\left(\Delta q_{FP}, \Delta \theta_{e,FP}, \Delta p_{FP}\right)}{\Delta T_{FP}} \qquad (17)$$

The subscripts EE and FP denotes how ΔT, $\Delta \theta_e$, Δq and Δp are computed. The closer the ratio is to 1, the more similar the accuracy is to that of the FLEXPART output data. An amount of less than 1 indicates an underestimation of the result computed by the energy equation and vice versa. The aim is not only to estimate the extent of driving processes but also to evaluate their errors and minimize them, if necessary. For instance, a numerical equation of θ_e or temperature-dependent latent heat of vaporization can be replaced in equation (12) (see e.g., Davis - Jones, 2009).

5 Results

All results are presented and discussed further on. The first subsection about the case study of the PNW June 2021 heat event includes a description of the synoptic situation and meteorological conditions. Furthermore, the origin and driving processes during the PNW June 2021 event are discussed. The most relevant findings with respect to the PNW June 2021 event are compared to those for the previous PNW events.

5.1 Synoptic situation during and before the PNW June 2021 event

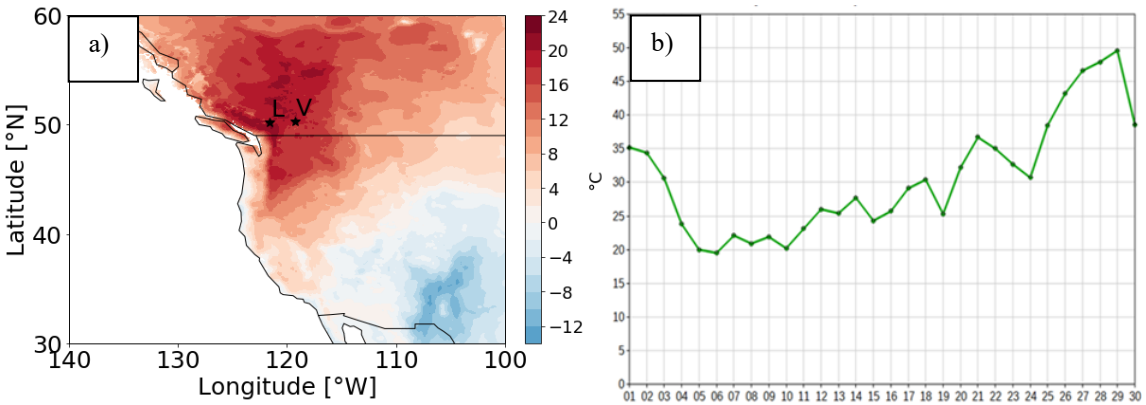

Figure 2. (a) Anomaly of summer daily maximum 2-m temperature on June 30, 2021, at 00 UTC (June 29, 5 pm PDT). 6-hourly ERA5-Land reanalysis data for season summer (JJA) from 1950-2021 are used. The geographical position of Lytton (L), where the highest absolute 2-m temperatures were recorded, and Vernon (V), from where two radiosondes' measurements on June 29 and June 30 are displayed in figure 4, are marked with a black star. **(b)** Daily maximum 2-m temperatures obtained from situ measurements in Lytton (PDT) for June 2021 (climate.weather.gc.ca).

On June 30, 2021, the daily maximum 2-m temperature shows anomalies above 20K in the Pacific Northwest (figure 2a). In addition, archives from an in-situ weather station at Lytton show an increase in daily maximum 2-m temperature that began on June 25 and continued for five consecutive days through June 30. The previous Canadian all-time temperature record of $45.0°C$, measured in 1937 (climate.weather.gc.ca), was broken in Lytton three days in a row during the peak of the heat event. ($46.6°C$, $47.9°C$, $49.6°C$; see figure 2b). The end of the PNW June 2021 heat wave is visible by the daily maximum 2-m temperature of about 38°C on

the day after the peak. Although the daily maximum temperature on July 1 was more than $10\ K$ lower than on June 30, this value is still far above the climatological mean. Thus, Lagrangian analysis data are evaluated on July 1, 2021, as well as during the event peak.

First insights about the onset and course of the PNW June 2021 event are provided by the geopotential height and equivalent potential temperature θ_e at 500 hPa and 850 hPa height from June 23 to June 30, 2021 (figure 3). The start of the PNW June 2021 heat event is noticeable by a northeastward transport of extraordinary warm air mass ($\theta_e > 65°C$ in 500 hPa) within a baroclinic zone over the northern Pacific on June 23. In further course a warm conveyor belt (WCB) started to form and warm air mass in 500 hPa height began to enter the mainland of Canada on June 24. The warm air mass continued to intrude into a persistent quasi-stationary upper-level omega block, in which the air mass was trapped and circulated anticyclonically during the following days. Usually, the climatological JJA-mean of θ_e in 500 hPa height over the Pacific Northwest is about $45°C$, depending on the exact region. The θ_e values of the trapped air mass within the anticyclone ranged from $60°C$ to $65°C$ on June 25, up to $20\ K$ above the climatological mean. Additionally, the potential temperature started to increase in 850 hPa over the affected area within the anticyclone on June 26, a situation that indicates descent. Moreover, an upper-level mesoscale low over the northeastern Pacific intensified in 500 hPa on June 27 and June 28 due to substantial gradients of θ_e. Further increase of θ_e in 850 hPa over the Pacific Northwest contributed to a baroclinic instability. Consequently, a pressure drop (about $40\ gpm$ in 24 h) occurred within the mesoscale low on June 29. The mesoscale low shifted slowly northeastward and enhanced easterly wind in about 850 hPa over parts of the Pacific Northwest during the peak of the heat wave. Any connections between the easterly wind, Foehn effects and the occurrence of extreme near surface temperatures within the affected region, including valleys in southern British Columbia are examined and discussed in the next subsection.

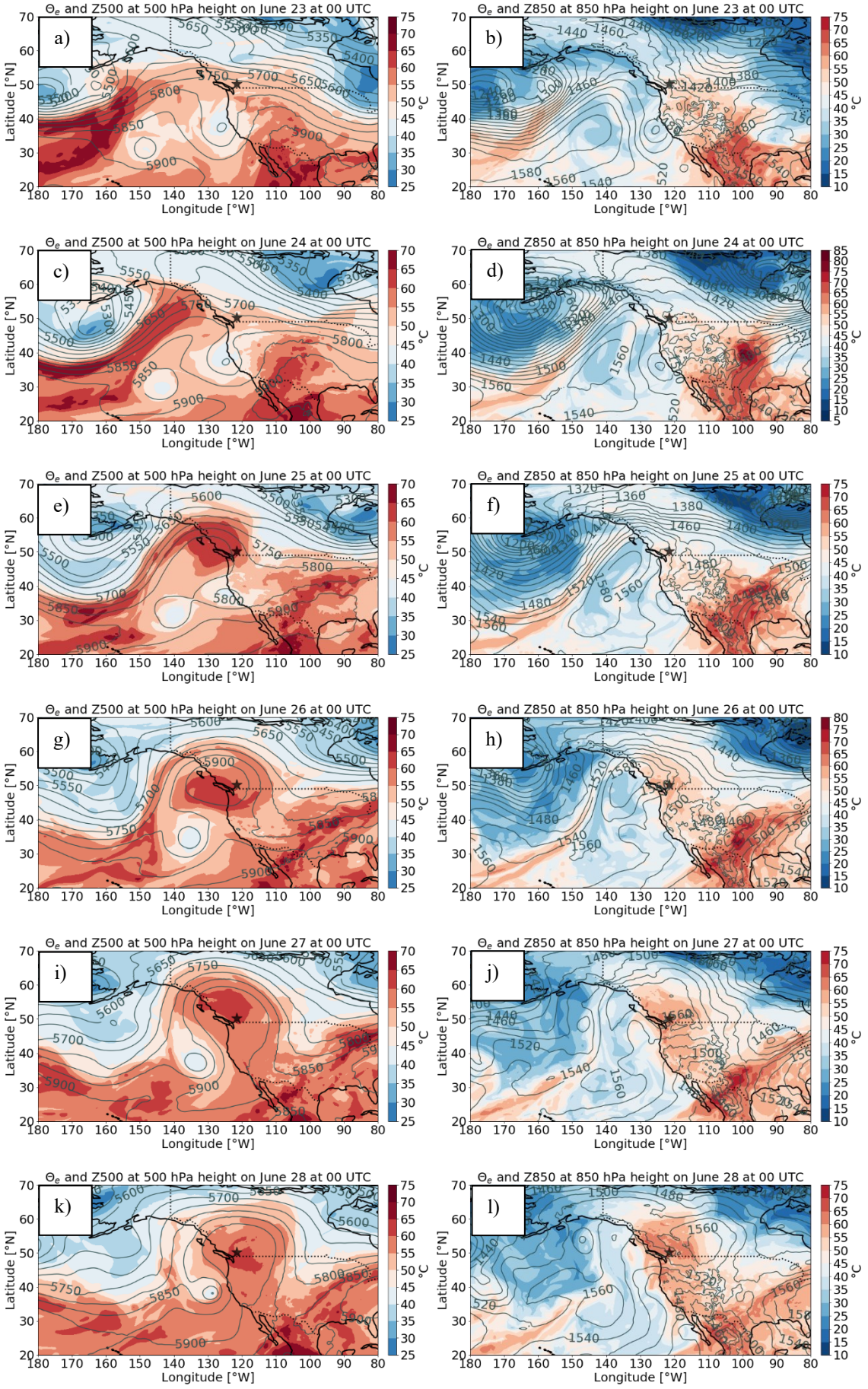
Θe and Z500 at 500 hPa height on June 23 at 00 UTC
a)
Θe and Z850 at 850 hPa height on June 23 at 00 UTC
b)
Θe and Z500 at 500 hPa height on June 24 at 00 UTC
c)
Θe and Z850 at 850 hPa height on June 24 at 00 UTC
d)
Θe and Z500 at 500 hPa height on June 25 at 00 UTC
e)
Θe and Z850 at 850 hPa height on June 25 at 00 UTC
f)
Θe and Z500 at 500 hPa height on June 26 at 00 UTC
g)
Θe and Z850 at 850 hPa height on June 26 at 00 UTC
h)
Θe and Z500 at 500 hPa height on June 27 at 00 UTC
i)
Θe and Z850 at 850 hPa height on June 27 at 00 UTC
j)
Θe and Z500 at 500 hPa height on June 28 at 00 UTC
k)
Θe and Z850 at 850 hPa height on June 28 at 00 UTC
l)
Latitude [°N]
Longitude [°W]
°C

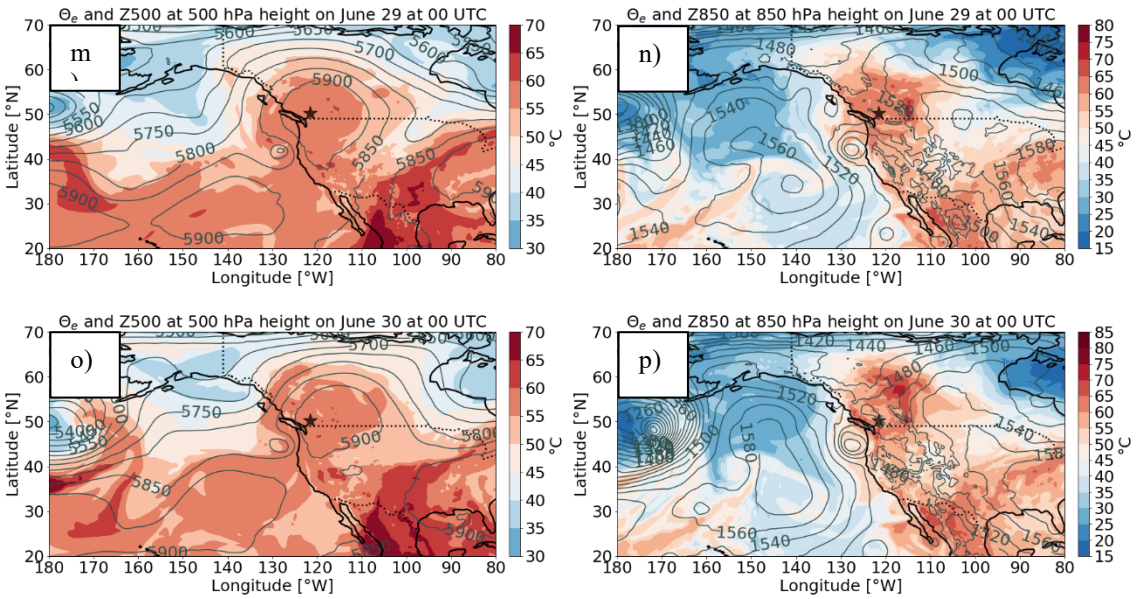

Figure 3. The equivalent potential temperature, θ_e (colored shading), and the geopotential height, *Z (black isolines),* are shown at 500 hPa on the left side in **(a), (c), (e), (g), (i), (k), (m)** and **(o)** and at 850 hPa on the right side in **(b), (d), (f), (h), (j), (l), (n)** and **(p)** by using ERA5 reanalysis data on pressure levels. The geograhical position of Lytton is marked as a black star. The JJA climatological mean (1971 – 2021) of θ_e ranges from about $40 - 45\ °C$ in 500 hPa height over the Pacific Northwest.

Further important meteorological parameters like the PBL height, moisture or stratifications are illustrated in radiosonde measurements that started from Vernon on June 29 and June 30, 2021, at 2315 UTC (figure 4). The easterly wind is also visible in the wind flags of the radiosonde measurement between 700 hPa and 800 hPa height, which started from Vernon on June 29 (figure 4a). Since the Rocky Mountains are located to the east of Vernon, possible Foehn effects would be considered as another factor in the development of extreme near surface temperatures. Nevertheless, the similarity of the temperature profile on June 30 without any easterly wind flags rather argues against any Foehn effects as one of the main driving processes. Additionally, the unusually high boundary layer top is higher than most of the highest peaks of the Rocky Mountains and thus higher than any valleys in which descent by Foehn effects may occur. According to the gradient method (e.g., Liu & Liang, 2010) the PBL height is recognizable by the simultaneous appearance of the dry adiabatic temperature lapse rate in the lower troposphere and a sudden decrease of the dewpoint (decrease of mixing ratio) at the PBL top. These criteria identify a PBL height of about $650\ hPa$ $(3{,}500 - 4{,}000\ m)$

over Vernon on June 29 and June 30 (figure 4), which is less than the easterly wind flags in $700 - 800\,hPa$ (greater than $2{,}000 - 3{,}000\,m$) height. Consequently, it is out of the question that additional adiabatic heating by Foehn effects occurred within a mixing layer, which would not have been driven to such a great height without the presence of the high mountain peaks of the Rocky Mountains and dry soils.

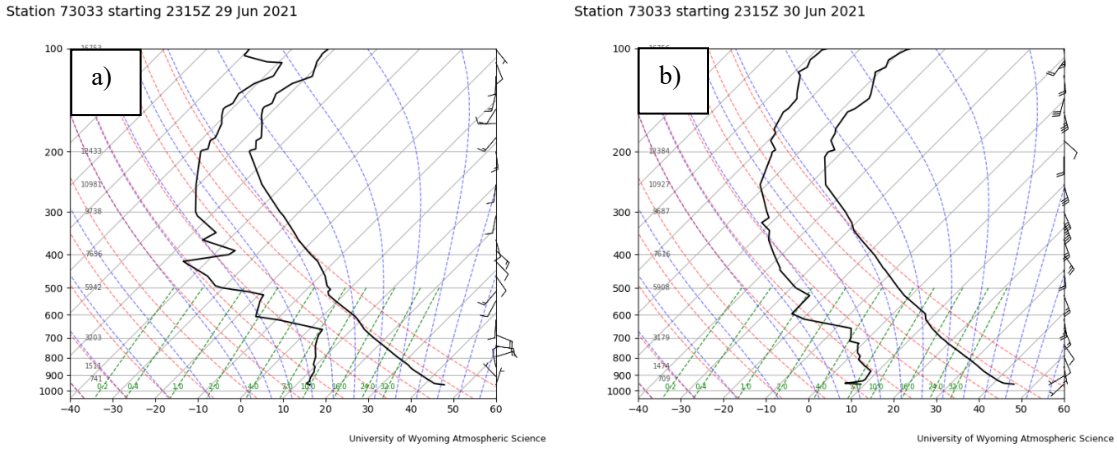

Figure 4. Skew-T-diagrams showing measurements of the radiosonde started in Vernon (73033) on June 29 at 23:15 UTC, **(a)**, and on June 30 at 23:15 UTC, **(b)**. The tephigrams display the vertical profiles of temperature, dewpoint, wind speed and wind direction. Note: local time is Pacific Daylight Time (PDT = UTC – 7h).

Another aspect that becomes visible through the temperature and dewpoint profiles is low relative humidity that is estimated by the differences between dewpoint and temperature (spread). The spread was about $20 - 30\,K$ throughout the entire troposphere on June 29 and June 30, which corresponds to a relative humidity of about $10 - 25\,\%$. The lowest values occurred near the ground and above the PBL top. Even the lowest spread at the PBL top itself was about $10\,K$ or greater, a value that inhibits any formation of clouds that would lead to reflection of significant portions of incoming shortwave radiation. That intense insolation is indicated by the super-adiabatic temperature lapse rate of $2 - 3\,K$ near the ground on both radiosonde measurements as well. Moreover, the 2-m relative humidity were not only below about 20% in Vernon, but also over a widespread area over southern parts of the Canadian provinces British Columbia, Alberta and the western United States (figure 5b).

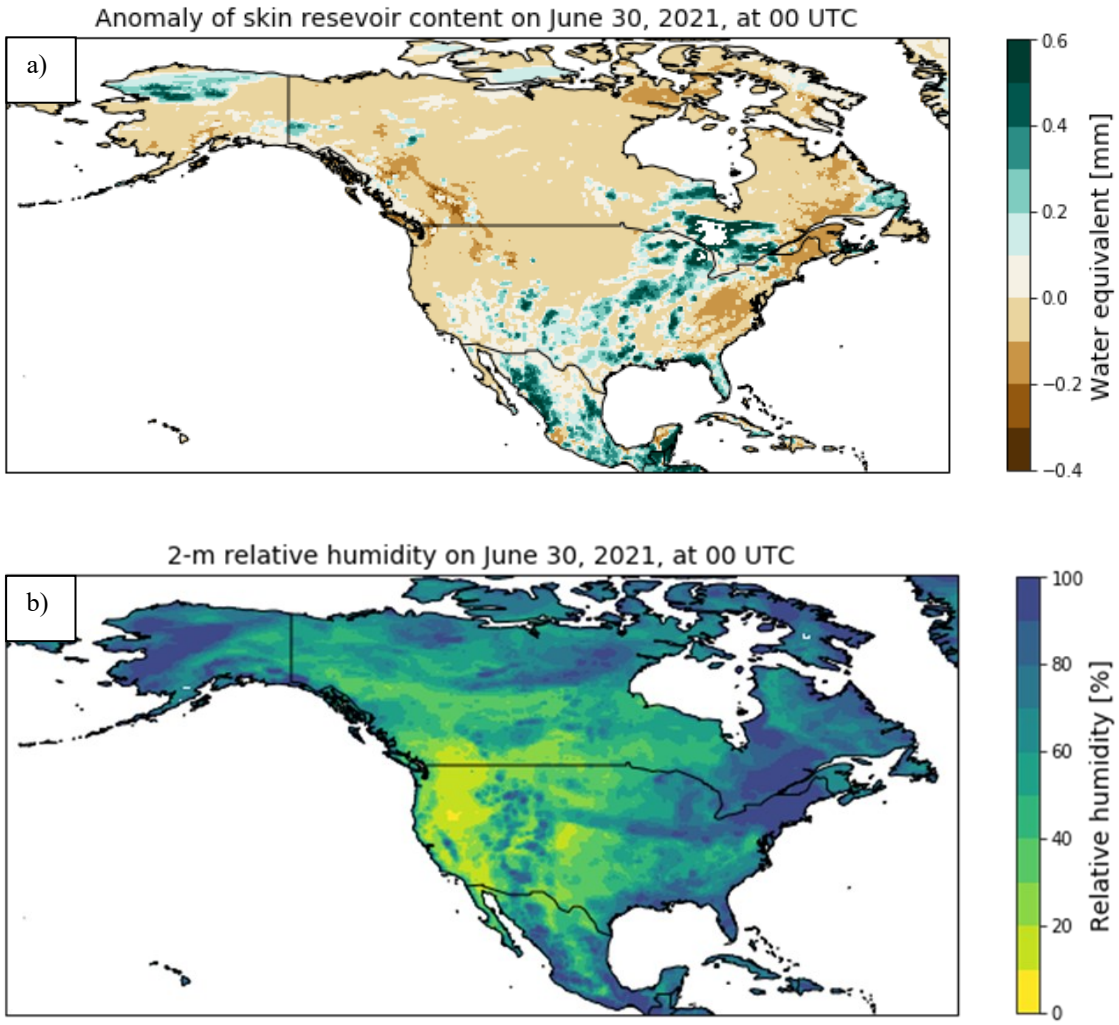

Figure 5. Moisture conditions during the PNW June 2021 event. The skin reservoir contents (ERA5), moisture that is available for evaporation, are shown in figure **(a)** as a 1950-2020 anomaly at the beginning of the PNW June 2021 event (June 25, 2021). The 2-m relative humidity is calculated by Magnus-formula using ERA5 data and is plotted in figure **(b)** during the peak of the event (June 30, 2021).

The observed low relative humidity and high PBL top could be a consequence of the absence of evaporation due to dry soils. Lower evaporation restricts cooling latent heat fluxes and thus the entire incoming energy is partitioned towards sensible heat (Seneviratne et al., 2010). To pursue other indications of any positive soil-moisture-temperature feedback, ERA5 data of skin-reservoir content anomalies at the beginning of the PNW June 2021 event, on June 25, are illustrated in figure 5a. Here, negative anomalies of the skin reservoir content are visible over widespread areas of North America. Especially, the amount of water equivalent available for evaporation was far below the climatological mean over the Pacific Northwest. According to Phillip et al. (2022) low snow cover, early snow melt and

low precipitation amounts from April to June 2021 contributed to such a low soil moisture at the beginning of the PNW June 2021 event on June 25. Ultimately, the observed dry conditions favored not only the development of high near surface temperatures, but also provides favorable conditions for onsets of widespread wildfires, including the destructive fire in Lytton (see Fire Weather Index in e.g., Van Wagner, 1987).

Thus, to summarize, large amounts of exceptional warm air was transported across the northeastern Pacific and trapped within a blocking high for at least five days. Furthermore, the increase of potential temperature in 850 hPa emphasizes descending air mass, in which potential energy is converted into sensible heat that contributes to 5-sigma near surface temperature anomalies in late June 2021. In addition, the air was entrained into an extraordinarily high PBL during the PNW June 2021 event. As mentioned before, low soil moisture caused positive soil-moisture-temperature feedback, thus leading to the exceptionally high PBL height and 2-m temperatures (Seneviratne et al., 2010). Moreover, it is very unlikely that additional adiabatic heating by Foehn effects occurred during the PNW June 2021 event.

5.2 Energy transport during the PNW June 2021 heat event

In the following, I present the results of the Lagrangian FLEXPART analysis during the PNW June 2021 event to reveal important driving processes or origins of air mass that are not fully resolved by the Eulerian results before. The Lagrangian output data calculated by FLEXPART are illustrated as frequency distributions (as particles' 5th, 25th, 50th, 75th and 95th percentiles) up to 15 days backward in time (figure 6, 7, 9, 10) and represent the meteorological and physical conditions of air mass during arrival. The first question that is addressed here is from where the air mass came from and how the transport patterns of zonal, meridional and vertical components had changed before arrival.

In general, all particles originated from warmer regions south and west of the release box over Lytton (figure 6). More than 75% of all particles were located at least south of latitude 40°N 10 to 15 days prior to the release date. More accurately, about 50 % of all particles arrived from a region between about the latitudes 10°N and 20°N and between the longitudes 120°E and 160°E 15 days before the highest absolute 2-m temperatures were measured over the PNW on June 30 (figure 6e, f). Furthermore, a not negligible part of the air mass was located near the ocean surface (figure 7). Thus, most of the surface fluxes could only have occurred over the sea surface of the Pacific Ocean, as indicated by the zonal and meridional movement of air mass before the PNW June 2021 event.

As the particles' density distribution in figure 8a confirms, a large portion of the air arriving on June 30 was previously located over the subtropical western Pacific south of Japan on June 18, 2021. About $50\ \%$ of all air mass were located below $2{,}500\ m$ (figure 8b) over sea surfaces with temperatures over $25°C$ 12 days before the arrival on June 30. Connections with the extraordinary high sea surface temperatures around the origin and any moisture uptake before the unprecedented PNW June 2021 event seems likely, which is indicated by high values of θ_e. $50\ \%$ of the air on backward day 12 had equivalent potential temperatures between $57°C$ and $77°C$ on backward day 12 before the arrival on June 28, from $62°C$ to $80°C$ before June 29 and from $65°C$ to $82°C$ before the event peak on June 30 (figure 10). High amounts of moisture and thus high values of θ_e provide favorable

conditions for the development of intense heatwaves if latent heat is released during the transport towards the midlatitudes.

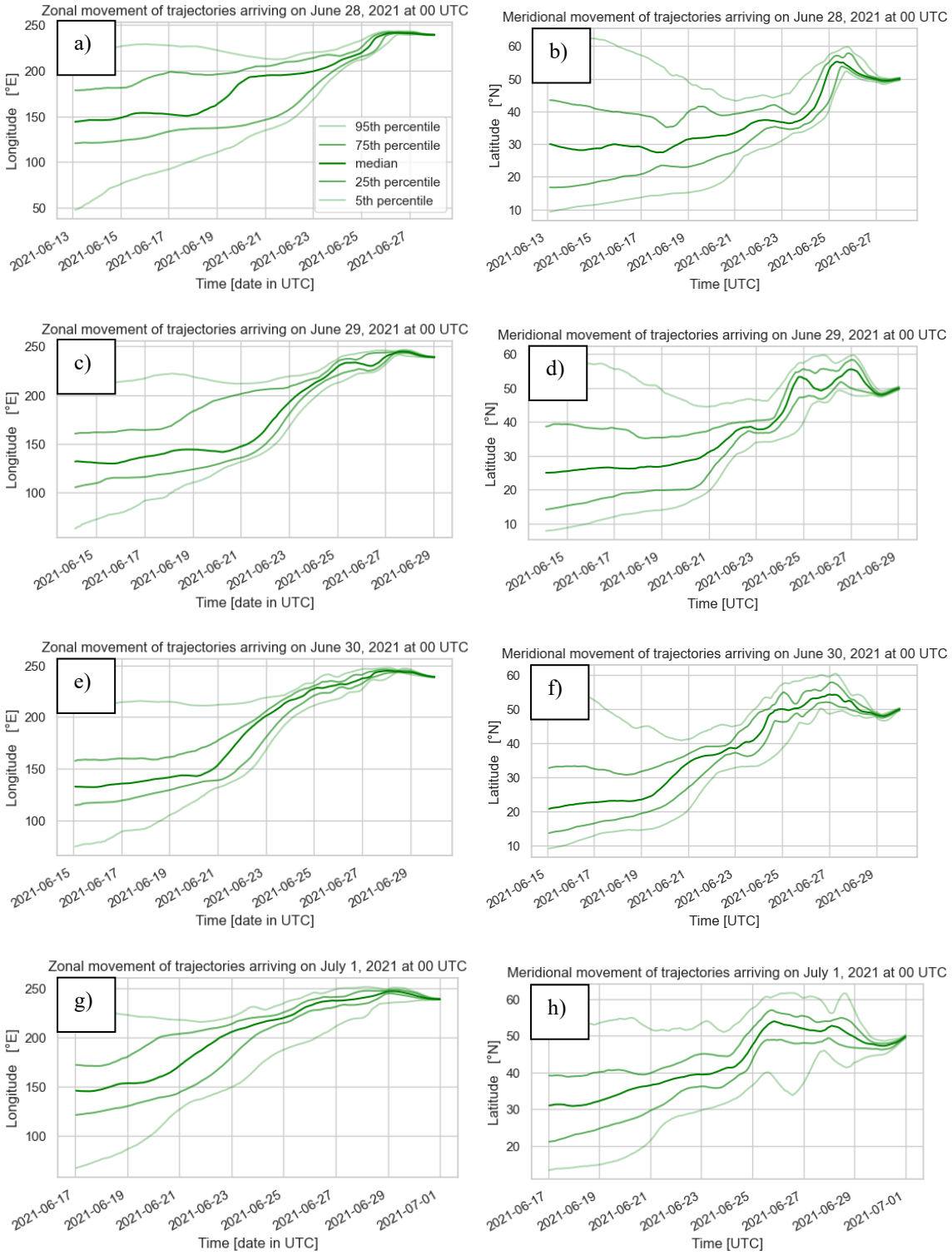

Figure 6. The zonal (left panels) and meridional (right panels) movements of trajectories starting from Lytton are shown as the trajectories' 5th, 25th, 50th, 75th and 95th percentiles (see legend in **(a)**) over 15 days backward in time. The release time of the Lagrangian analysis data range from June 28 to July 1, 2021, at 00 UTC.

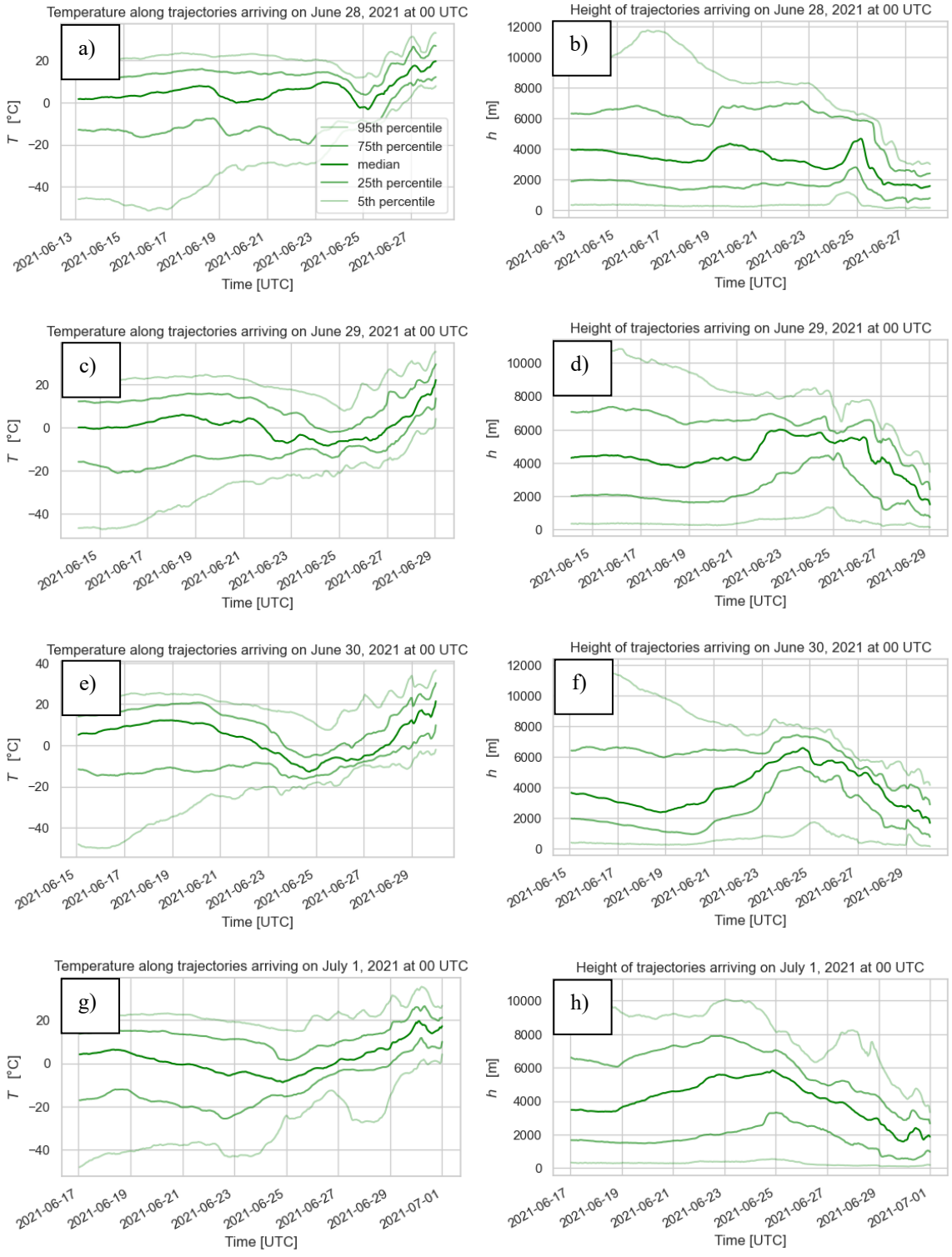

Figure 7. Frequency distribution (legend in **(a)**) of the temperature (left panels) and height above ground level (right panels) along 15-day back trajectories starting from Lytton. The green-shaded solid lines represent the particles' 5th, 25th, 50th, 75th and 95th percentile. The trajectory release dates are reported on the top of each panel. Data above range from June 28 to July 1, 2021, at 00 UTC.

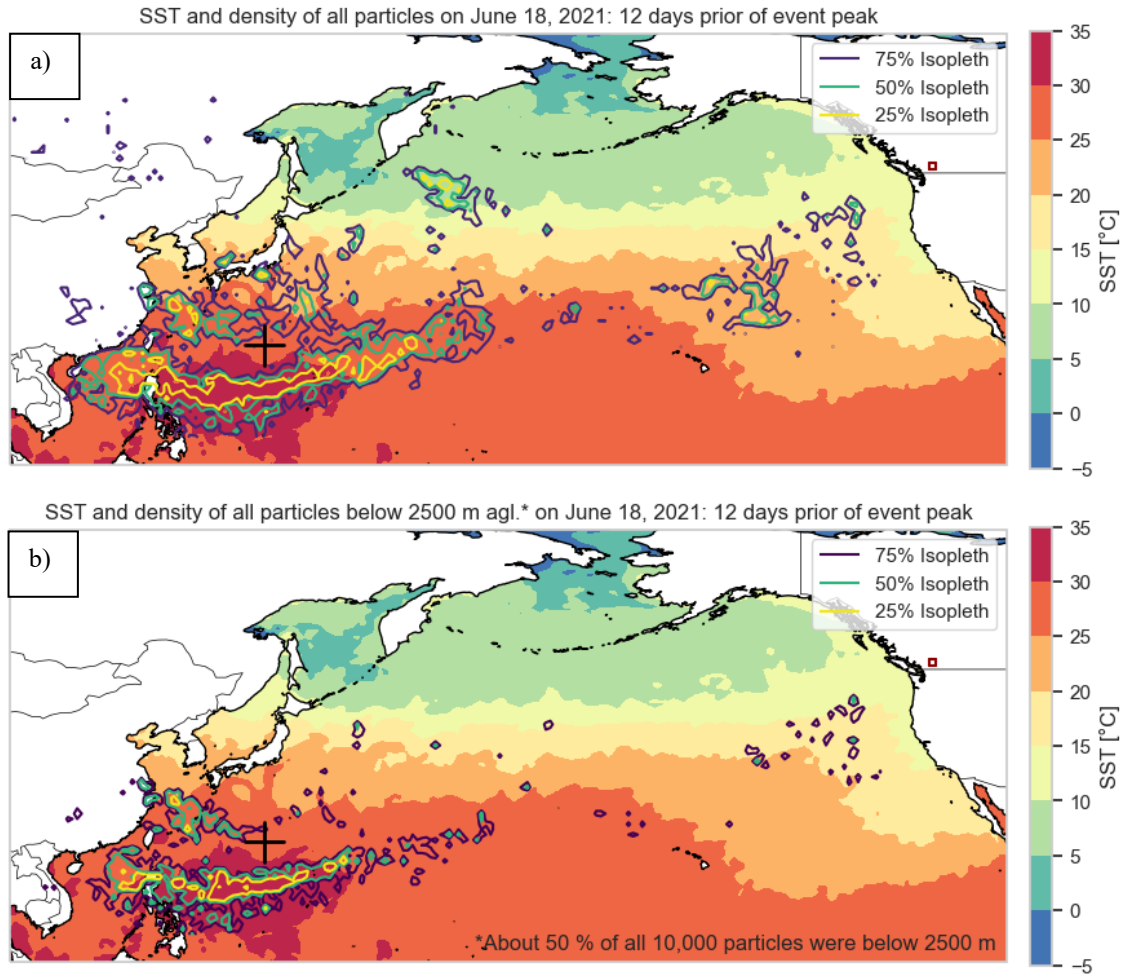

Figure 8. SSTs and the particles' position as density contour lines on June 18, 2021, at 00 UTC, 12 days prior of the release date on June 30, 2021, at 00 UTC. The density of all particles is shown in **(a)**, whereas the density of particles that were below 2,500 m is given in **(b)**. The percentages 25%, 50% and 75% denote the portion of all 10,000 particles in **(a)** and of all about 5,000 particles in **(b)**. The particles' median of longitudes and latitudes on June 18 is marked as a black plus sign. DOISST v2.1 data are used to illustrate the SSTs as a colormap. The solid dark red line over southern British Columbia encloses the particle release box.

5.3 The role of preceding latent heat release

Furthermore, an increase of specific moisture to up to $20\ g\ /\ kg$ occurred until about the tenth backward day before arrival on June 28, 29 and 30 (figure 9). Moisture in the vapor phase can decrease by condensation, a process that releases latent heat. A comparison of the evolution of potential temperature, height and specific humidity helps to identify the processes which lead to diabatic heating. For instance, when the ascent of air was strongest on June 19 before the arrival on June 28, an increase in potential temperature and a simultaneous decrease in specific humidity (figure 9) indicates latent heat release by condensation within precipitating clouds. In this subsection, I highlight trajectories of 5 individual diabatic heating cases (figure 11, 12 and 13) between the arrival dates from June 28 to July 1, which indicate latent heat release within ascending supersaturated air. Furthermore, the results are compared with the geographical positions, where significant amounts of precipitation fell within the respective time period, to verify the reason for latent heat release. In addition, the equivalent potential temperature is used to evaluate any exchange with the environment during the diabatic processes.

Starting from June 28 backward in time the particles' potential temperature increase and simultaneous moisture decrease took place from June 24 to June 26 (figure 9a, b) when the air mass was transported cyclonically and ascended along a warm conveyor belt at the beginning of the mentioned time period (figure 11a). A remarkable process is the transport across up to 20 degrees of latitudes in one day from June 24 to 25 (figure 6b). During the transport the equivalent potential temperature remained nearly constant (figure 10b) while the particles' median of potential temperature increases by about $7 - 8\ K$ and the particles' 95th and 75th – percentiles of specific moisture decrease by 3 – 5 $g\ /\ kg$ (figure 9a, b). Such changes verify latent heat release and indicate typical physical processes within air parcels moving along a warm conveyor belt (Eckhardt and Stohl, 2004), whose outflow usually affects regions along the mountain ranges of western North America. After about $50\ \%$ of air parcels ascended across a height of $5{,}000\ m$ above ground level within the warm conveyor belt, the parcels descended further downstream on the leeside of the mountain ranges on June 26 (figure 11a).

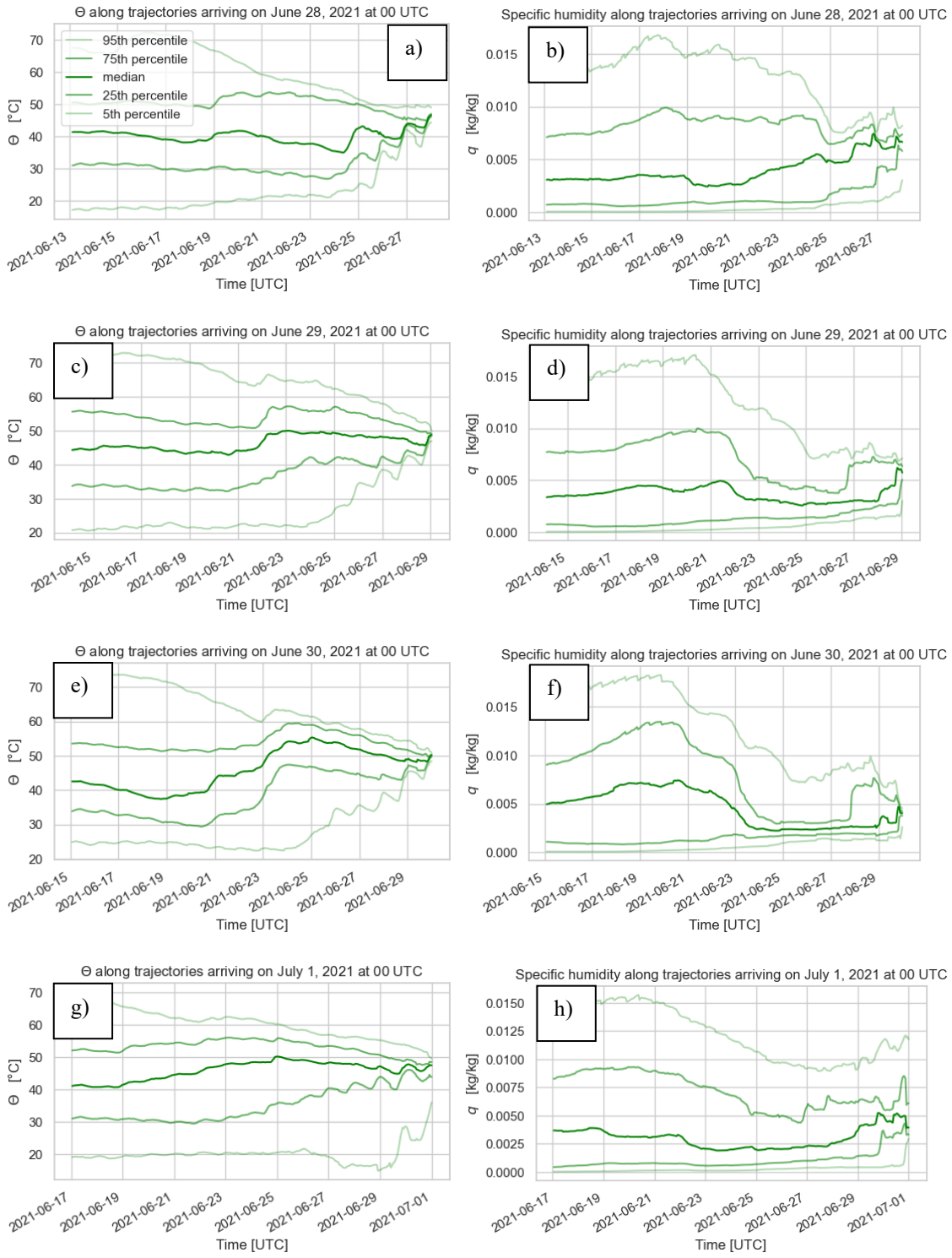

Figure 9. Frequency distribution (legend in **(a)**) of the potential temperature (left panels) and specific humidity (right panels) along 15-day back trajectories starting from Lytton. The green-shaded solid lines represent the particles' 5th, 25th, 50th, 75th and 95th percentile. The trajectory release dates are reported on the top of each panel. Data above range from June 28 to July 1, 2021, at 00 UTC.

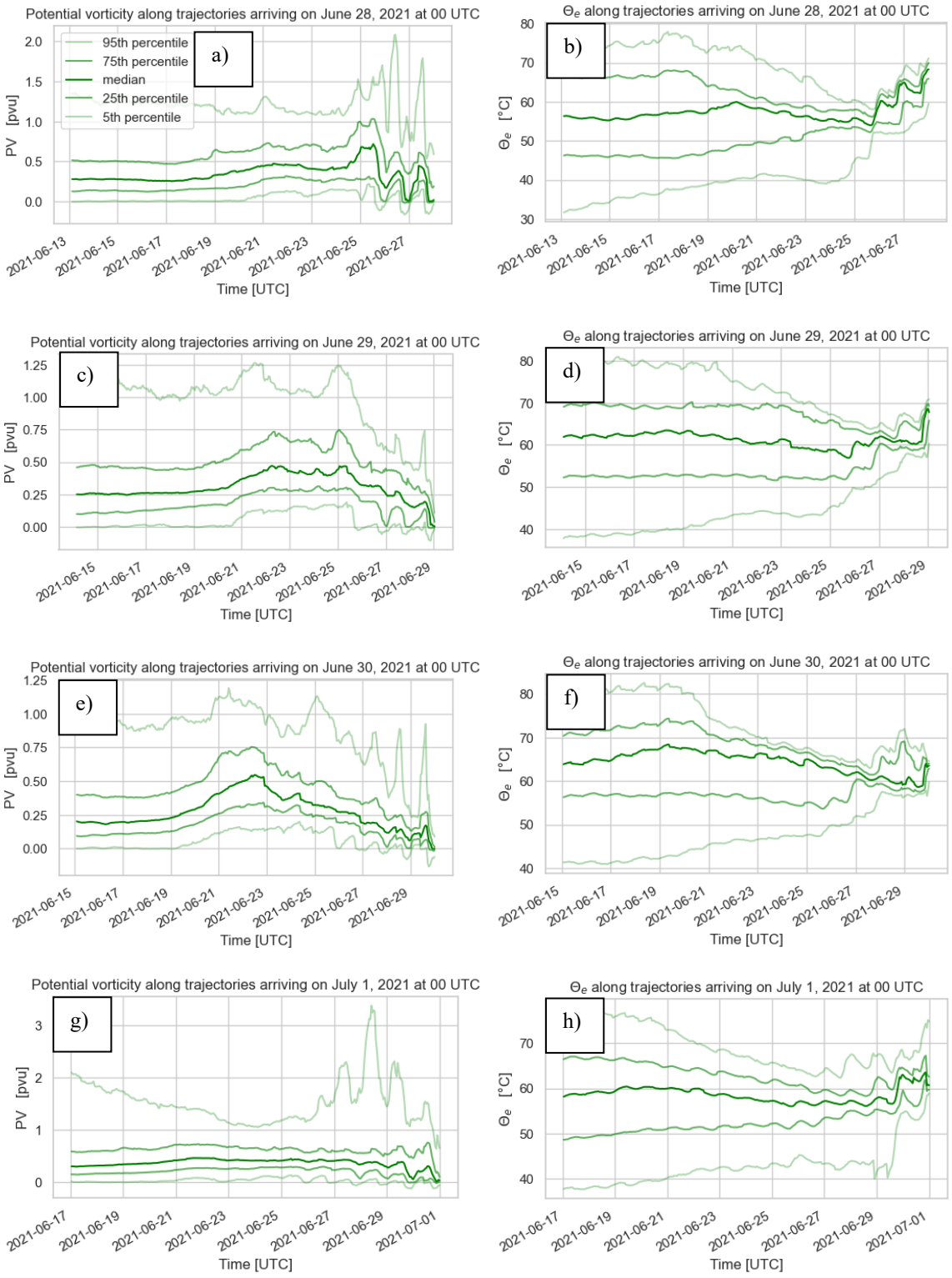

Figure 10. Frequency distribution (legend in **(a)**) of the potential vorticity (left panels), and the equivalent potential temperature, θ_e (right panels), along 15-day back trajectories starting from Lytton. Note the different scales of potential vorticity in **(a)** and **(g)**. The green-shaded solid lines represent the particles' 5th, 25th, 50th, 75th and 95th percentile. The trajectory release dates are reported on the top of each panel. Data above range from June 28 to July 1, 2021, at 00 UTC.

Another time of increase in potential temperature and decrease in specific moisture, which indicates diabatic heating by latent heat release, occurred between June 21 and June 23 along trajectories that arrived at Lytton on June 29 (figure 9c, 9d). During that time period the transport patterns were anticyclonically (figure 11b) which is usually associated with descent. A comparison with figure 7d clearly confirms the subsidence of air mass until June 19, but not within the depicted time period in figure 11b. At this point, it should be mentioned that the particles' percentiles include ascending as well as descending air parcels. If the portion of ascending (descending) air mass dominates the particles' percentiles of height would increase (decrease). In this case, one portion of air mass ascended within mesoscale convective clusters along the so called Meiyu-Baiu-Front while the other portion of air mass slightly descended downstream of the convective events, as figure 11b illustrates.

According to the particles' 1st, 2nd and 3rd quartiles, the height increased by up to $2{,}000\ m$ (figure 7d) while the potential temperature increased by about $8\ K$ (figure 8c) and the specific humidity decreased by up to $5\ g/kg$ (figure 9d). In addition, the approximately constant values of θ_e indicate closed systems during the latent heat release from June 21 to June 23 (figure 10d). Thus, the latent heat release is mainly caused by ascending supersaturated air mass over the subtropical western North Pacific from June 21 to June 23, 2021, which arrived at Lytton on June 29. Furthermore, it is worth to mention that the particles' 1st, 2nd, and 3rd quartiles of potential temperature start to increase from a higher value of θ before the arrival on June 29. Thus, the air parcels arrived with an about $2-3\ K$ higher potential temperature, although the air mass had been heated diabatically to a similar extent (about $8\ K$) before June 28 and June 29.

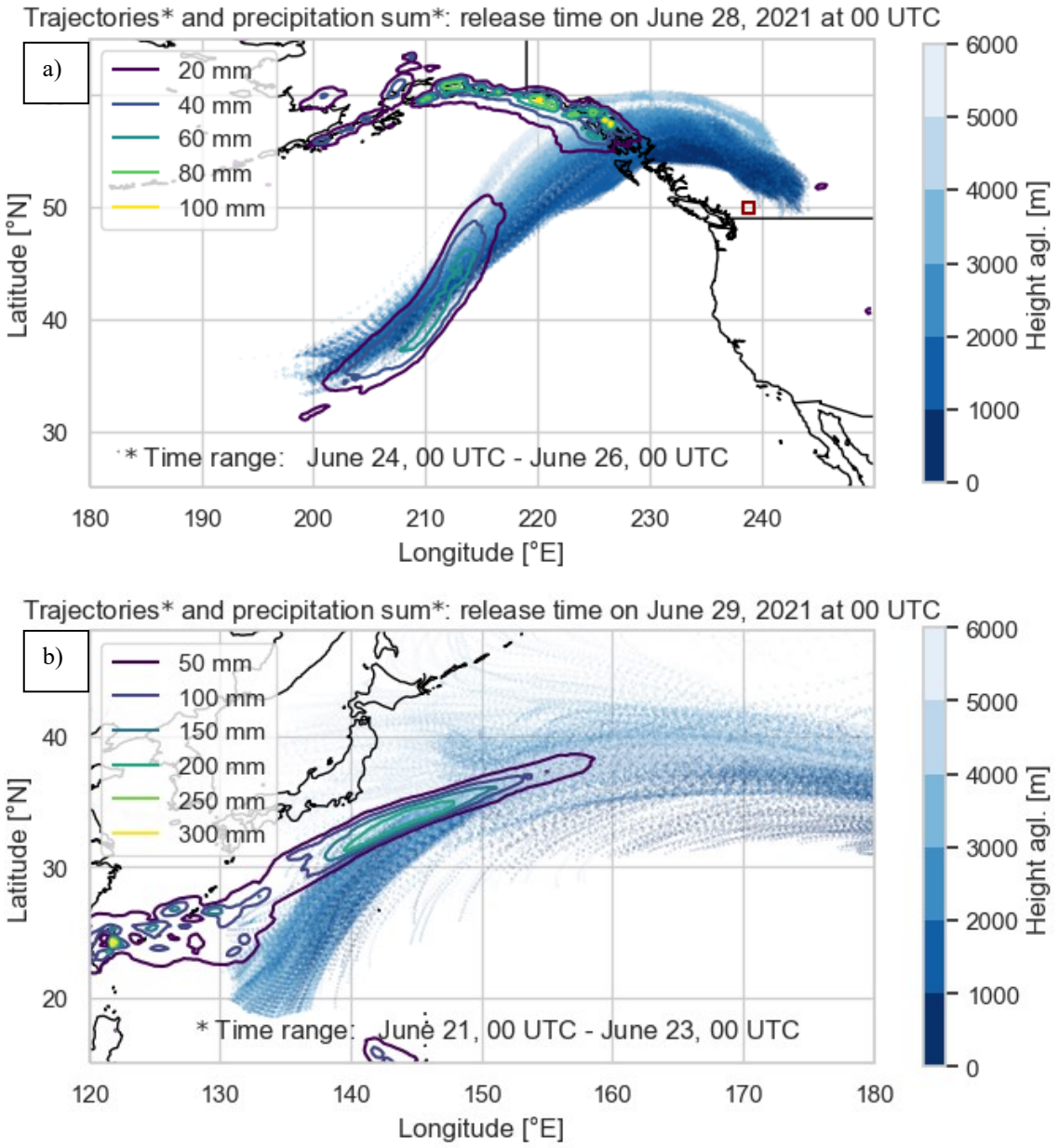

Figure 11. Trajectories (blue shaded lines) arriving around Lytton (red square) on June 28 **(a)** and 29 **(b)**, 2021, and the total precipitation amounts (green isolines, ERA5) within different chosen time ranges. The blue colors show the particle height. The following respective chosen time windows correspond to the strongest increase in potential temperatures (see figure 8a, 8c).

Before the air mass arrived Lytton on June 30, the potential temperature increased (figure 9e) along the Meiyu-Baiu-Front (figure 12a) from June 20 to June 22 and along a warm conveyor belt from June 22 to June 24 (figure 12b). In addition, the moisture decreased within the air mass during the same period from June 20 to June 24 before the peak of the PNW June 2021 event (figure 9f). First, the particles' 1st, 2nd and 3rd quartiles of height increase by up to $1{,}500\ m$ from June 20 to June

22 (figure 7f), despite of large-scale anticyclonic transport patterns south of the Meiyu-Baiu-Front (figure 12a). During the same time, the particles' 5th, 25th, 50th, 75th and 95th percentiles of potential temperature increase by up to $5\ K$ (figure 9e) while the percentiles of specific moisture decrease by up to $3\ g\ /\ kg$ (figure 9f). In contrast to the air mass, which are related to the arrival dates on June 28 and June 29, the equivalent potential temperature decreased within the air mass that arrived on June 30. Especially, the particles' 75th and 95th percentiles of θ_e decrease by up to $5\ K$ from June 20 to June 21 (figure 10f), which is more than the expected decline of $1\ K$ per day by outgoing longwave radiation. That could imply that some portion of air mass was located near cloud tops where higher cooling rates occur. However, the question about the reason of decline in θ_e is difficult to reveal in this framework.

After the air mass had been heated diabatically by latent heat release from June 20 to June 22, about 50 % of all air parcels remained within a layer between about $2{,}000\ m$ and $6{,}000\ m$ and shifted downstream towards the warm conveyor belt where they ascended before the arrival on June 30 (figure 12b). The strongest ascent of more than $3{,}000\ m$ is visible by the particles' 25th percentile of height from June 22 to June 24 (figure 7f) and occurred over areas where stratiform precipitation fell (figure 12b). The particles' 50th, 75th and 95th percentiles of specific humidity range from about $6\ g\ /\ kg$ to $14\ g\ /\ kg$ (figure 9f) on June 22 when the air parcels were located upstream of the warm conveyor belt. Furthermore, as the particles' 1st, 2nd and 3rd quartiles demonstrate, the potential temperature increased by about $5\ -12\ K$, while the specific humidity decreased by up to $8\ g\ /\ kg$ and the equivalent potential temperature decreased by the prementioned rate of $1\ K$ per day from June 22 to June 24 (figure 10e). This is typical for latent heat release within warm conveyor belts (Eckhardt and Stohl, 2004).

Overall, the particles' 1st, 2nd and 3rd quartiles of potential temperature totally increase by $15 - 20\ K$ from the minimum value on June 20 to the maximum on June 24 (figure 8e), while the particles' 95th, 75th and 50th percentiles of specific humidity totally decrease by about 10 g/kg (figure 9f) during the two precipitation events (figure 12). In comparison to the latent heat release that occurred within air parcels before their arrival on June 28 and June 29, the changes of both prementioned quantities were the greatest along trajectories that end in Lytton on June 30.

On this arrival date, the particles' mean potential temperature is about 50 °C, a value that would not have been possible without the latent heat release before. Therefore, the observed latent heat release is classified as one of the most decisive driving processes during the PNW June 2021 event.

Diabatic heating also occurred within air mass that arrived one day after the PNW June 2021 event peak on July 1 (figure 9g). During the latent heat release from June 19 to June 23, the height and potential temperature increased more slightly until the arrival on July 1. According to the particles' 1st, 2nd and 3rd quartiles, the height increased by about $1{,}000\,m$ to $2{,}000\,m$ (figure 7h) while the potential temperature increased by about $2 - 10\,K$ (figure 9g) and the specific moisture decreased by about $2 - 5\ g/kg$ from June 19 to June 23 (figure 9h). The same particles' quartiles of θ_e decrease by about $1\,K$ per day during the same time period, which indicates closed systems during the processes like latent heat release within precipitating clouds. The comparatively smaller amount of diabatic heating is because smaller portions of air mass ascended within the precipitation events over the North Pacific (figure 13) from June 19 to June 23. Consequently, the particles' 5th, 25th, 50th, 75th and 95th percentiles of potential temperature are considerably smaller on the arrival date on July 1, which ranges from $35°C$ to $48°C$. In contrast, the particles' mean potential temperature ranges from $46°C$ to $50°C$ on the preceding release dates on June 28, 29 and 30, which approximately correspond to the in-situ measurements of daily maximum 2-m temperature in Lytton ($46.6°C, 47.9°C, 49.6°C$).

Not all air mass ascended diabatically, as a comparison of the particles' percentiles of height, temperature and potential temperature illustrate. For instance, the particles' 95th percentile of height related to the release date July 1 increases to about $8{,}000\,m$ from June 27 to June 28 (figure 7h) while all particles' percentiles of potential temperature remain approximately constant (figure 9h). A smaller portion of diabatically heated air mass that are related to the arrival date on July 1 also explains the lower observed in-situ 2-m temperature in Lytton on that day.

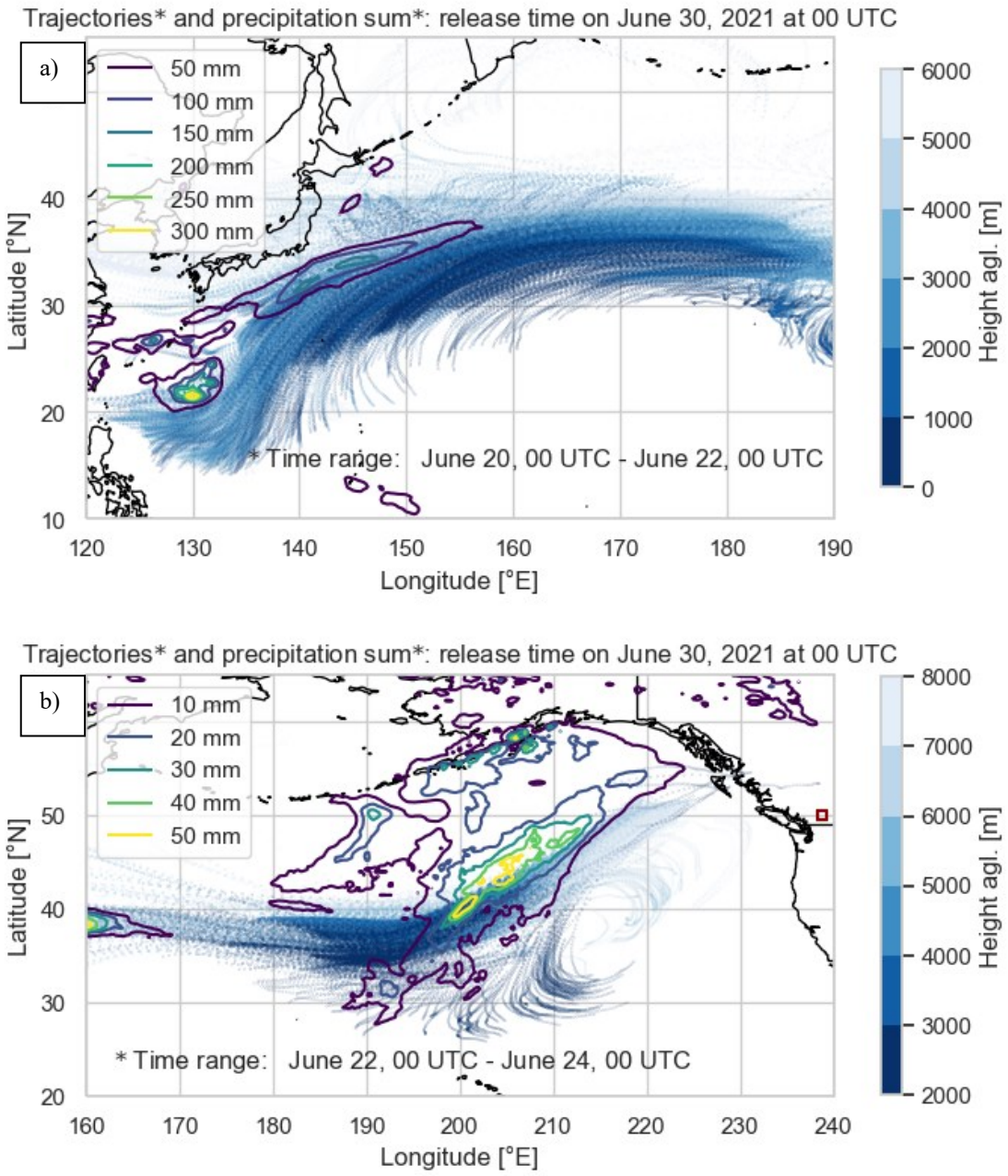

Figure 12. Trajectories (blue shaded lines) arriving around Lytton (red square) on June 30, 2021, and the total precipitation amounts (green isolines, ERA5) within different chosen time ranges from June 20 to June 22 in **(a)** and from June 22 to June 24 in **(b)**. The blue colors show the particle height. Note the different scale of height in **(b)** given by the color bar on the right side. The following respective chosen time windows correspond to the strongest increase in potential temperatures (see figure 8e).

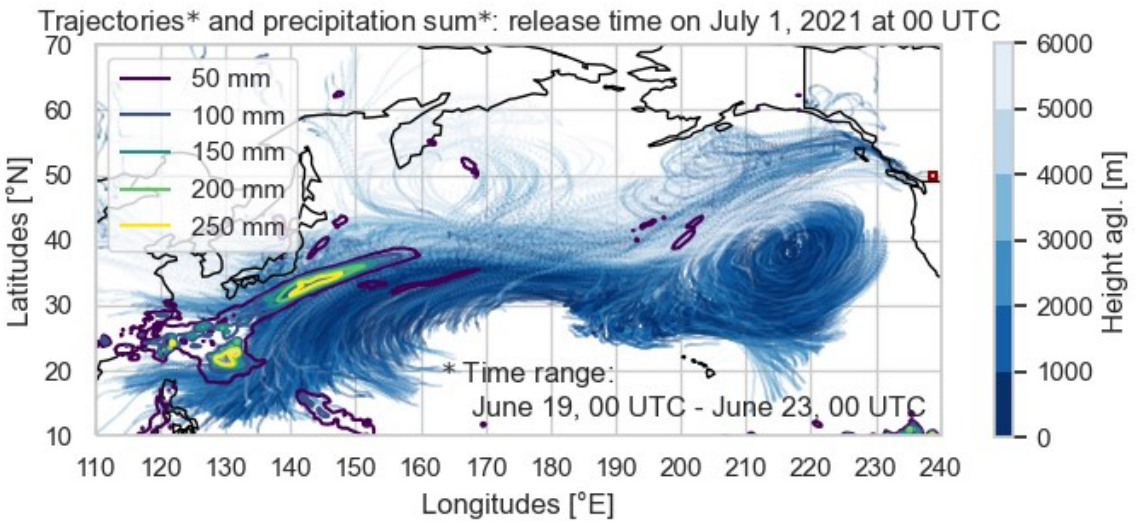

Figure 13. Trajectories (blue shaded lines) arriving around Lytton (red square) on July 1, 2021, and the total precipitation amounts (green isolines, ERA5) from June 19 to June 23. The blue colors show the particle height. The following respective chosen time windows correspond to the strongest increase in potential temperatures (see figure 8g).

5.4 Adiabatic heating during the PNW June 2021 heat event

The five depicted cases of latent heat release (figure 11, 12 and 13) further demonstrate their importance to the development of an atmospheric blocking, in which the potential temperature is converted into sensible heat by subsidence. This fact is corroborated by the increase of the observed total adiabatic heating until the respective release date from June 28 to June 30.

Since the particles were released from the same altitudes, the extent of adiabatic heating due to subsidence is indicated by the maximum point of the particles' percentiles of height. The maximum of the particles' 1st, 2nd and 3rd quartiles of height range from $3{,}000\ m$ to $7{,}000\ m$ in figure 7b, from $4{,}500\ m$ to $7000\ m$ in figure 7d and from $5{,}500\ m$ to $7{,}500\ m$ in figure 7f. Thus, the air parcels' descent depth increased from the arrival date on June 28 until June 30. This is also reflected by the changes in the particles' median of temperature, which increases by about $20\ K$ until June 28, about $30\ K$ until June 29 and about $35\ K$ until June 30 within the preceding 5 days. The air mass released on July 1 descended from a similarly high level as well, according to figure 7h, but not as fast as during the PNW June 2021 event peak.

Furthermore, using the definition of the dynamical tropopause threshold of 2 potential vorticity units ($1\,pvu = 10^{-6} K\,m^2 kg^{-1} s^{-1}$) (Ertel, 1942), the particles' 95th percentile of the potential vorticity relating to the arrival date on July 1 also indicates that some air could have ascended across the troposphere and descended from a stratospheric level on June 28 (figure 10g). In fact, the methods and values of the stratospheric threshold are controversial and other definitions of the tropopause height exist (e.g., Kunz et al., 2011). For instance, the thermal tropopause definition of $330\,K$ or the dynamical tropopause definition of $3.5\,pvu$ are also commonly used to define the height of the lowermost stratosphere in midlatitudes (e.g., Hoskins, 1985; Škerlak et al., 2014). Comparing the particles' 95th percentile of potential temperature (figure 9g) and potential vorticity (figure 10g) on June 28 before the arrival of air mass on July 1, the highest value of potential temperature is about $330\,K$ $(57°C)$ while the highest value of potential vorticity is about $3.3\,pvu$, $0.2\,pvu$ less than the alternative dynamical definition. Otherwise, the gradient method would not confirm any crossing of the tropopause, because the particles' 95th percentile of height and the particles' 5th percentile of temperature indicates a continuous negative temperature lapse during the considered time period (figure 7g, 7h). Thus, the highest layer from which some air descended is more likely the tropopause, but not from the stratosphere.

5.5 The role of typhoon Champi

The role of typhoon Champi and any impact on the air mass that arrived at Lytton on June 30 deserves to be evaluated and reviewed in a separate subsection. According to the Japanese Meteorological Agency (JMA), a tropical storm named Champi originated over Micronesia on June 20, shifted northeastward during intensification to a category 1 typhoon (980 hPa core pressure) until June 25. The track of Champi changed to northeast, transformed into an extratropical storm, weakened and finally dissipated on June 28 (figure 14). The greatest amount of precipitation fell not only along the storm's eye, but also along the Meiyu-Baiu-Front where up to 500 mm precipitation fell during the lifetime of Champi. Such an amount of precipitation can be additionally enhanced by the impact of a tropical storm during an extratropical transition (Bieli et al., 2019). Comparing the sea

surface temperatures, the track of Champi and the precipitation patterns southeast of Japan, the extratropical transformation of Champi must have started at some time after June 25, when the typhoon left areas with sea surface temperatures above $28°C$. Any convective clouds that had arisen by the influence of typhoon Champi could have contained some portion of the diabatically heated air parcels related to the PNW June 2021 event.

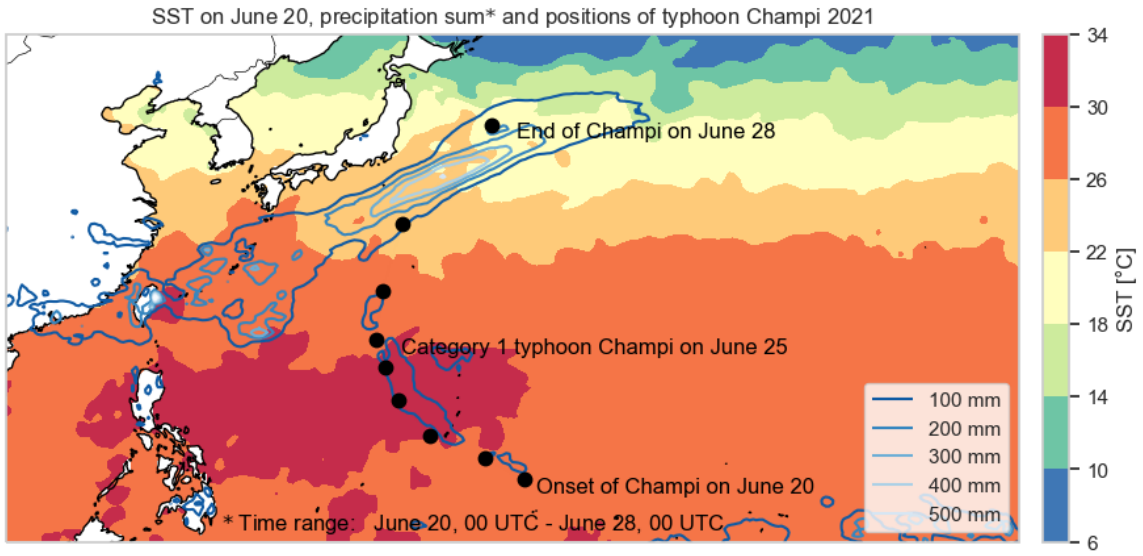

Figure 14. Storm track and sum of precipitation (ERA5, JMA) during the lifetime of typhoon Champi from June 20 to June 28, 2021. The colors represent sea surface temperatures on June 20, 2021, using DOISST v.2.1. data.

First indications about possible impacts by Champi are provided by a frequency distribution of orthodromes which illustrate distances between the particles' positions and the location of Champi's minimum pressure (figure 15b). As the particles' median of orthodromes shows, the closest distance between the air parcels and Champi was during the onset of the typhoon on June 20 and June 21, but not during the extratropical transition on June 25. During the closest distance, about $25\ \%$ of all particles were closer than $2{,}000\ km$ and only a small portion of about $5\ \%$ were closer than about $1{,}500\ km$ to Champi. To exclude any impact, the 850 hPa wind fields are compared additionally with the storm's and air parcels' positions when they were closest to Champi on June 21 (figure 15a). The locations of most of the backward traced particles are in the vicinity of regions with intense precipitation along the Meiyu-Baiu-Front on June 21, but far away from regions where wind fields are affected by the typhoon. Nevertheless, the typhoon

circulation may have supported convergence over the Philippine Sea and enhanced convection on the southeastern edge of the Meiyu-Baiu-Front, where only a few air parcels were in the vicinity (figure 13a). Otherwise, about $90\ \%$ of all particles are located between about $8{,}000\ km$ and $13{,}000\ km$ away from the center of Champi during the extratropical transition on June 25. To conclude, any influence of Champi cannot be detected.

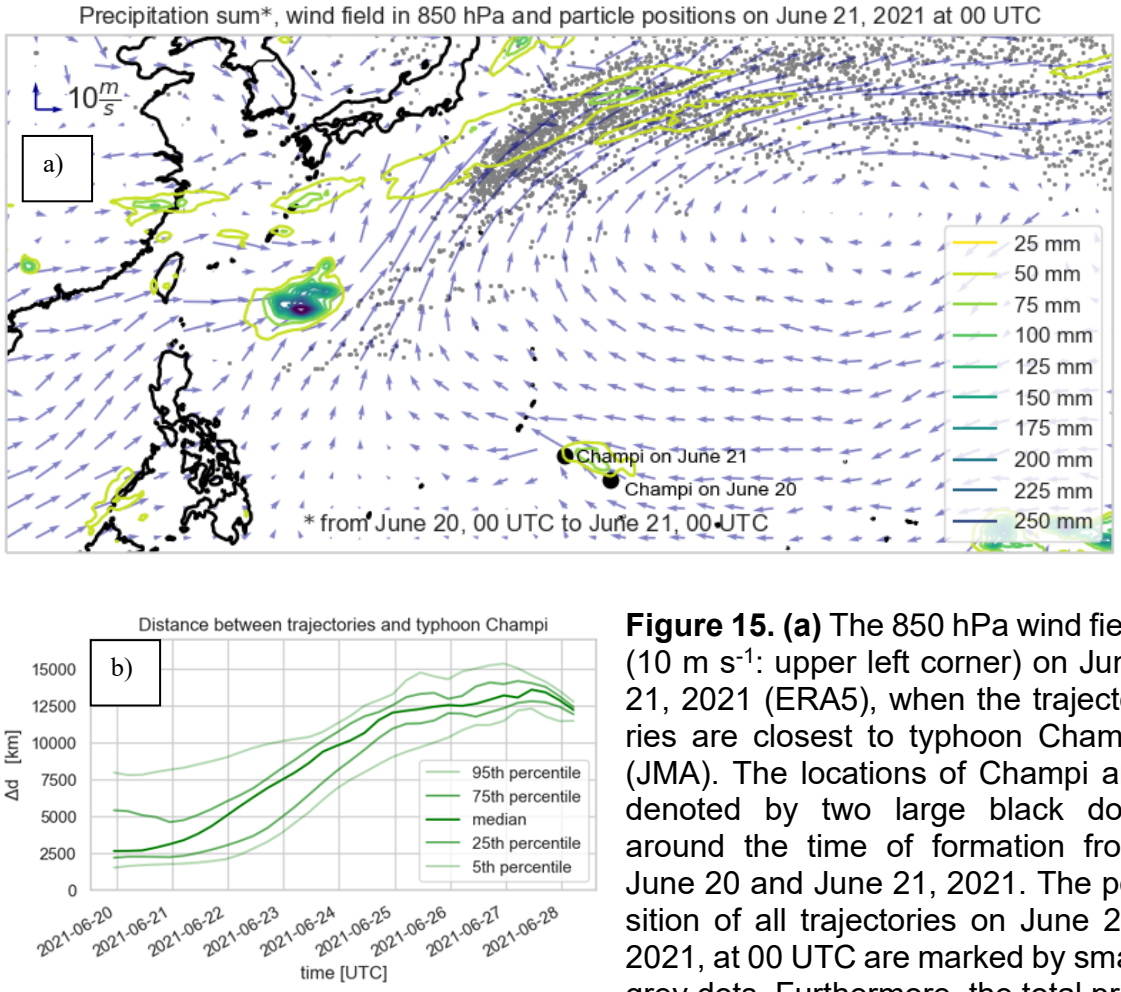

Figure 15. (a) The 850 hPa wind field (10 m s^{-1}: upper left corner) on June 21, 2021 (ERA5), when the trajectories are closest to typhoon Champi (JMA). The locations of Champi are denoted by two large black dots around the time of formation from June 20 and June 21, 2021. The position of all trajectories on June 21, 2021, at 00 UTC are marked by small grey dots. Furthermore, the total precipitation amounts between June 20 and June 21 are shown as green shaded contour lines. **(b)** Evolution of orthodromes (see legend), distances between the 2021 typhoon Champi and the air parcels, released on June 30, 2021.

5.6 Energy transport during PNW heat events

To address the question about any differences between air mass origin before each PNW event, the predominant climatology of θ_e is compared with the particles' geographical position 12 days before their arrival in Lytton. As the summer (JJA) climatology within the time period from 1971 to 2021 illustrate, the equivalent potential temperature increases not only to the south, but also to the west, especially within an area about from latitude 10°N to 40°N and about from longitude 120°E to 200°E (figure 16). Since a large portion of air mass originated from the prementioned area in the western Pacific Ocean before the PNW June 2021 event, it is also justified to evaluate the source region of air mass prior to other PNW heat events.

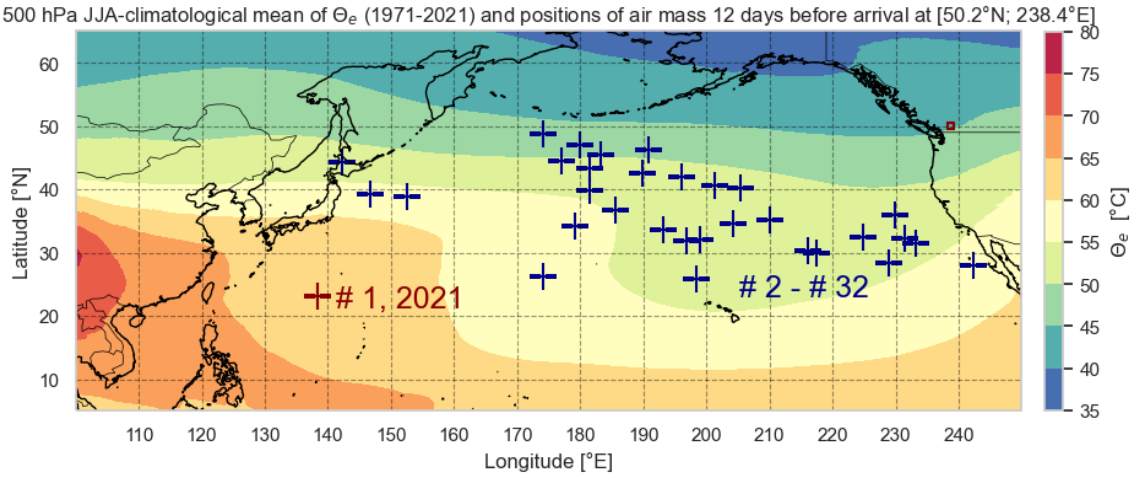

Figure 16. Climatological mean of θ_e in 500 hPa height between 1971 and 2021 for JJA by using ERA5 reanalysis data. The dark red and dark blue plus signs represent the trajectories' median of latitudes and longitudes 12 days before the respective PNW event took place. The solid dark red rectangular over southern British Columbia encloses the particle release box.

Obviously, the trajectories' median of zonal, meridional and vertical movement indicates decisive differences regarding the location of air mass before the PNW June 2021 event and previous PNW heat events (figure 17a, 17b). For none of the other cases did the air mass come from such a southern and western region (figure 16) and was at such a low altitude (figure 18a) on backward day 10 as for the PNW 2021 heat event. The particles' median latitudes of those three events, in which the

particles' median longitudes are about as far west as 12 days before event #1, are about $15° - 20°$ latitudes farther north at the same time than the particles' median latitude of event #1. Similar remarkable differences are visible for the particles' median longitudes of event # 1 and the particles' median longitudes of those events, in which the particles' median latitudes are south of latitude 30°N, on backward day 12. Consequently, the θ_e climatology shows about $5 - 15\ K$ higher values around the source region of event # 1 than around the origin of all other previous PNW heat events (figure 16).

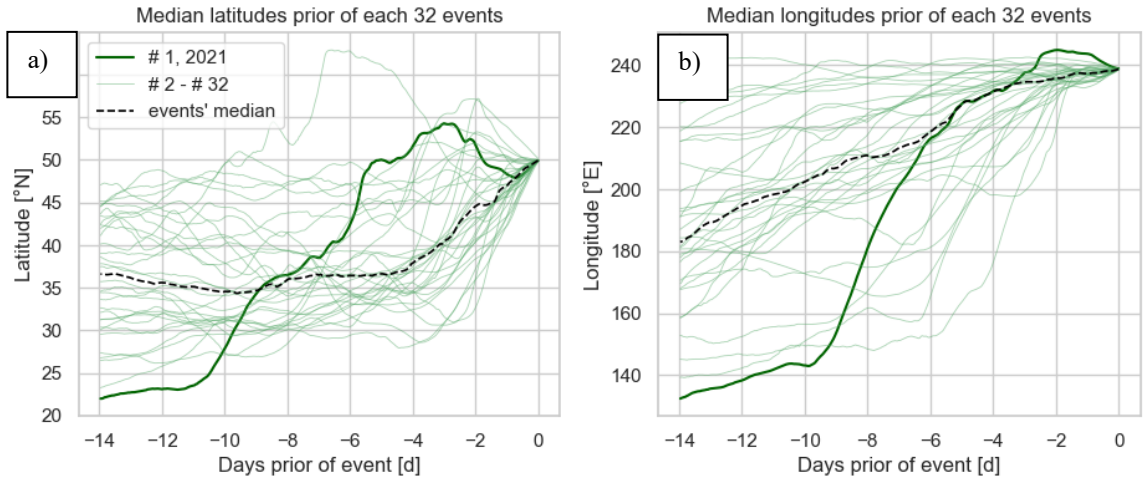

Figure 17. The temporal evolution of trajectories' median meridional and zonal movement during all considered PNW events are shown in panel **(a)** and **(b)**. The PNW June 2021 event is shown by a bold solid green line. The black dashed line on each panel represents the median of all identified PNW events. Each release date is during the respective peak of the PNW event.

Furthermore, about 50 % of all air mass were located below $2{,}500\ m$ on backward day 11 only during event # 1, whereas this portion of air mass ranged from about $3{,}800\ m$ to about $7{,}800\ m$ above ground level 11 days prior to all other events (figure 18a). The other 50 % portion of all air parcels were above the prementioned altitudes on backward day 11 and thus higher temperatures and any sea-surface-air-parcel interactions are most likely during event # 1. As it is expected in accordance with the height, the trajectories' median of temperature during the PNW June 2021 event is about $10\ K$ above the second highest and about $20\ K$ above the events' median on backward day 10 (figure 18b).

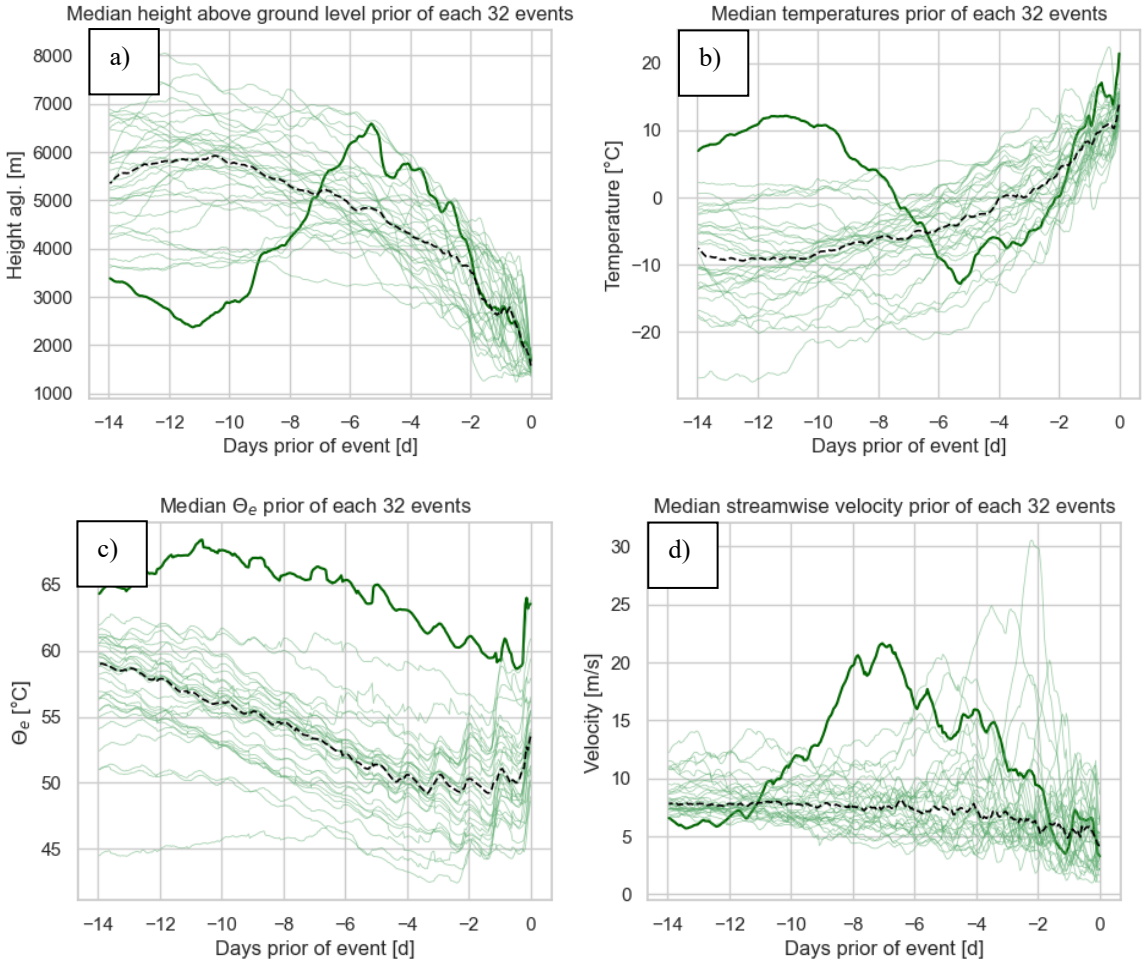

Figure 18. The temporal evolution of trajectories' median height **(a)**, temperature **(b)**, θ_e **(c)** and the streamwise velocity **(d)** during all considered PNW events. The PNW June 2021 event is shown by a bold solid green line. The black dashed line on each panel represents the median of all identified PNW events. Each release date is during the respective peak of the PNW event.

Since warmer air can take up more water vapor, it is also a reasonable approach to evaluate the specific moisture along the trajectories to reveal differences. Indeed, the trajectories' median specific moisture during the PNW June 2021 event is about 6 $g\ /\ kg$ greater than those trajectories' medians related to previous PNW events on backward day 8 and before (figure 19b), consistent with the climatologically warmer origin. In addition, the particles' median θ_e during event # 1 is about $10 - 12\ K$ higher than those during previous events from the moisture uptake on backward day 12 to the event peak (figure 18c). Moreover, the origin from climatological warmer regions of the # 1 event's air parcels can only be explained by a

higher transport velocity. As it is visible by the particles' median of streamwise velocity, the air mass arrived at a velocity between 10 and $20\ m/s$ from backward day 11 to 2 before event #1, which is far above the events' median transport velocity of about $8\ m/s$ (figure 18d). Ultimately, the considerably faster displacement of air mass along a warm conveyor belt before the PNW June 2021 event facilitates the transport from such a southern, western, warmer and more humid region.

5.7 Diabatic processes during PNW heat events

Differences in diabatic processes within air parcels during the PNW events are described in this subsection. According to the trajectories' median, the potential temperature increases by about $18\ K$ (figure 19a), while the specific humidity decreases by about $5\ g\ /\ kg$ (figure 19b) only before the PNW June 2021 event from backward day 11 to 5. During the same time period, the trajectories' median pertaining to the PNW 2021 event ascends by about $4{,}000\ m$ from backward day 11 to 5 and descends subsequently by about $5{,}000\ m$ from backward day 5 to the event peak (figure 18a). Consequently, the trajectories' median of potential temperature related to the PNW June 2021 starts from about $11\ K$ below the events' median potential temperature on backward day 11 and exceeds it by about $8\ K$ until June 30, 2021 (figure 19b). Ultimately, these different diabatic processes indicates in accordance with a warm conveyor climatology (Eckhardt & Stohl, 2003) that the transport of a significant portion of air mass along a warm conveyor belt must have occurred only before the PNW June 2021.

In contrast to the PNW June 2021 event, the potential temperature decreased while the specific moisture increased. During the preceding 10 days before the most of other PNW events the particles' median of potential temperature decreased by about $1\ K$ per day while the specific humidity remained approximately constant and increased during a few days before the events' peak. The air parcels started to descend from about $4{,}000\ m$ to $8{,}000\ m$ during most of all events from backward day 10 to the event peak (figure 18a). This corresponds to the prementioned cooling rate, which is caused by longwave outgoing radiation.

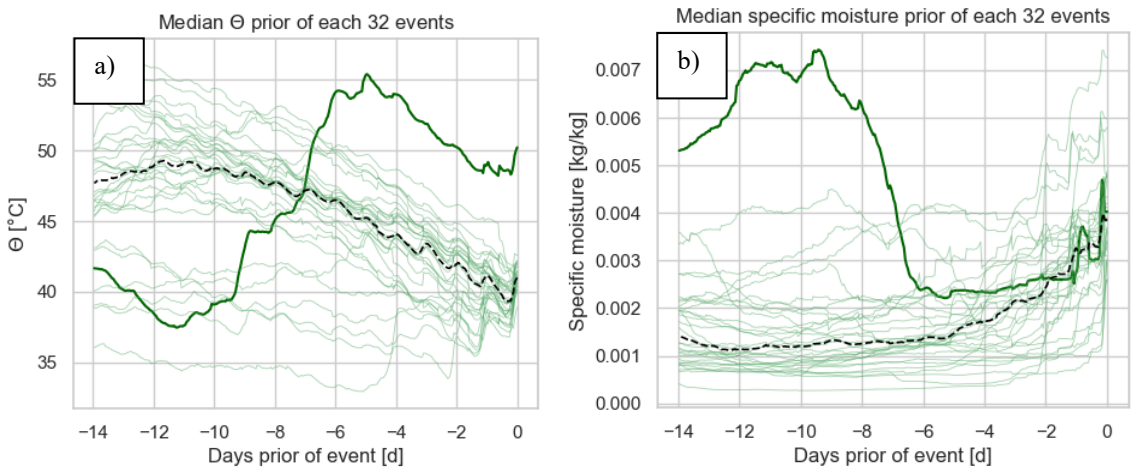

Figure 19. The temporal evolution of trajectories' median potential temperature and specific moisture during all considered PNW events are shown in panel **(a)** and **(b)**. The PNW June 2021 event is shown by a bold solid green line. The black dashed line on each panel represents the median of all identified PNW events. Each release date is during the respective peak of the PNW event.

Furthermore, I examine whether diabatic heating also occurred before previous PNW heat events or not. Air mass are also heated diabatically before five other PNW heat events. According to figure 20, the particles' mean net change of the potential temperature within a time period of 15 days is over $12\ K$ during the PNW June 2021 event and ranges from about $5\ K$ to $9\ K$ during event # 13, # 20, # 26, # 30 and # 32. Therefore, the events' mean driving processes of all those events are evaluated separately and are denoted by $\Delta\theta_{net} > 4K$ in figure 21. The events' mean processes of all other PNW events, where the particles' mean net change of θ is less than $4\ K$, are shown on the right side in figure 21. The particles' mean driving processes within 10 days (figure 21a) and 5 days (figure 21b) prior to the PNW June 2021 event peak are illustrated on the left-hand side of the panels.

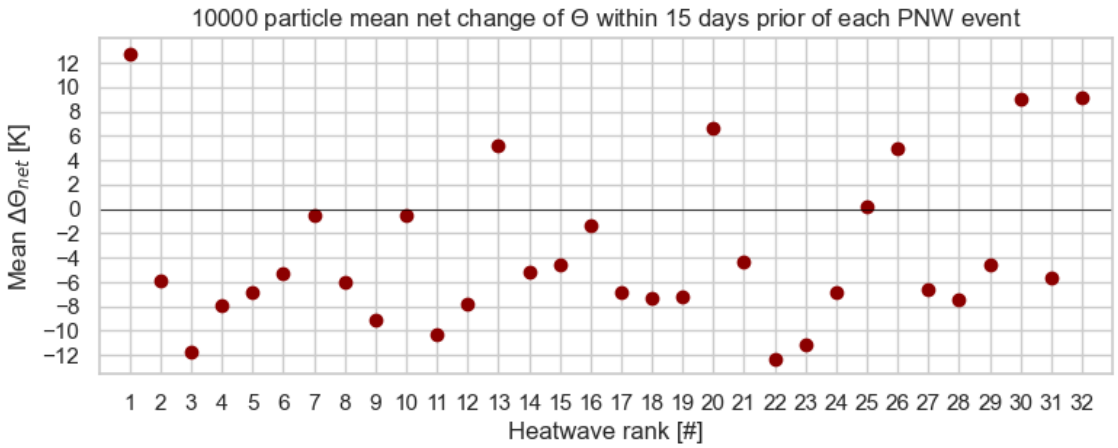

Figure 20. Trajectories' mean absolute net change of potential temperature is considered within 15 days prior of each PNW event peak. The scatterplot is utilized to demonstrate why the threshold of $4\ K$ is used for in figure 21.

As figure 21a illustrate, the value of the particles' mean temperature was about $5°C$ 10 days before the arrival on June 30, 2021, which is about $8\ K$ higher during events with $\Delta\theta_{net} > 4K$ and about $14\ K$ higher during events with $\Delta\theta_{net} < 4K$. The deviation of about $14\ K$ can be explained by the different sings of the particles' mean temperature change contributed by changes in specific moisture during the PNW June 2021 event ($\Delta T_{\Delta q} \approx 8\ K$) and during other events with $\Delta\theta_{net} < 4K$ ($\Delta T_{\Delta q} \approx -6\ K$). Such compositions of driving processes cannot be done in such a way for events with $\Delta\theta_{net} < 4K$ because any contributions to the particles' mean temperature by θ_e are not negligible during events with $\Delta\theta_{net} > 4K$, including event # 1 in 2021. The extent to which the particles' mean temperature increased by θ_e is $7.2 \pm 1.8\ K$ (figure 21a) within a time period of 10 days before events with $\Delta\theta_{net} > 4K$. Since θ_e is proportional to $-\nabla \cdot F$, any convergence of fluxes F near and within the boundary layer are expected to be mainly responsible for diabatic heating during the preceding days before the event # 13, # 20, # 26, # 30 and # 32. To verify this, I highlight these events in figure 22 and discuss the contribution of θ_e to the potential temperature and temperature.

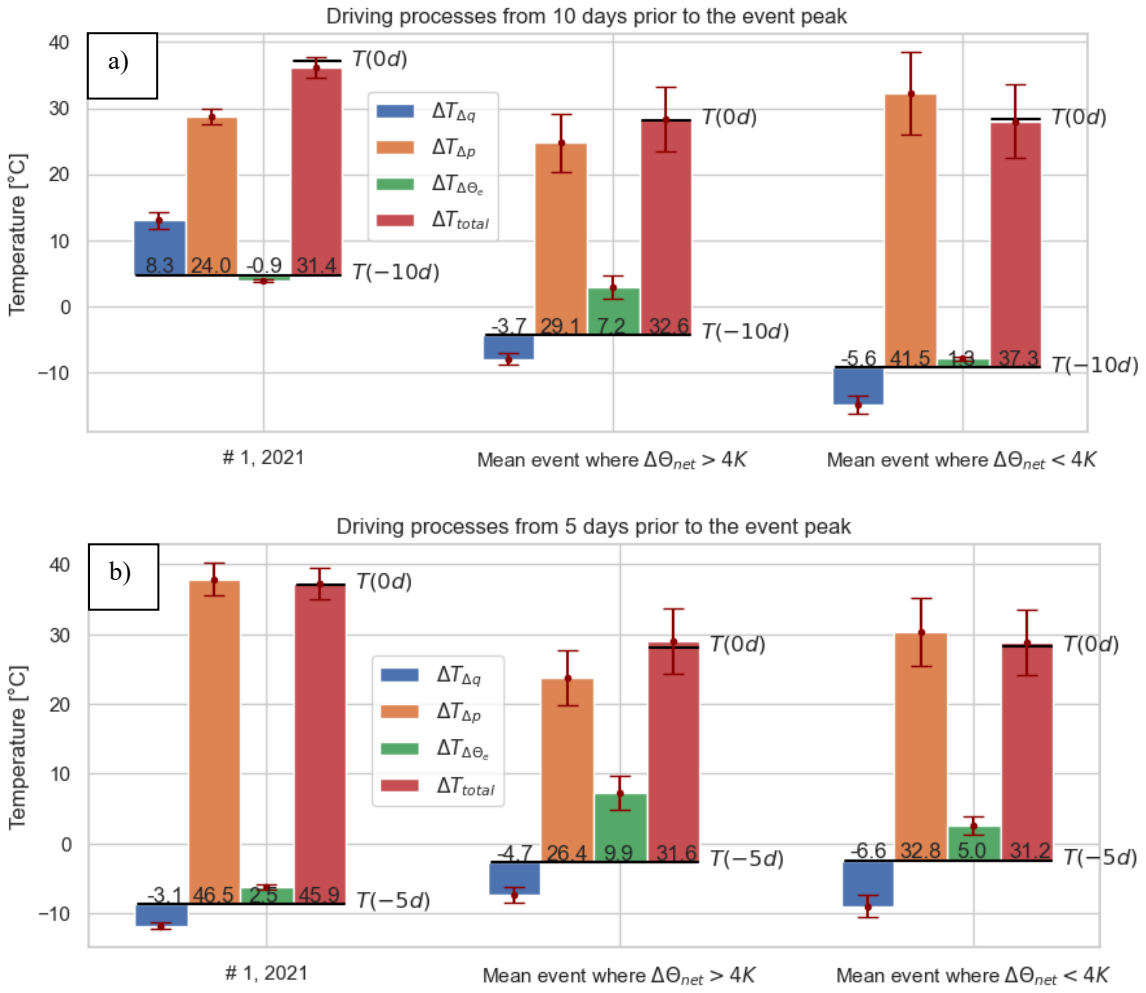

Figure 21. Trajectories' mean driving processes during PNW events within a time period from 10 days **(a)** and 5 days **(b)** to the time of each event peak. The total temperature change, T (red bars), include the changes of specific moisture, q (blue bars), changes of pressure, p (orange bars) and changes of the equivalent potential temperature, θ_e (green bars). All results obtained from the PNW June 2021 event are illustrated on the left side. The results of the events' mean driving processes during PNW events with $\Delta\theta_{net} > 4K$ are shown in the middle and events with $\Delta\theta_{net} < 4K$ on the right side (see figure 20.). The long black solid lines represent the trajectories' mean temperature of the FLEXPART output data 10 days prior, $T(-10d)$ in **(a)**, and 5 days prior, $T(-5d)$ in **(b)**, to the PNW heat event peaks. The numbers above each long black solid line represent the respective contributions to the total temperature change, given in K. The particle's mean temperature and the events' mean temperature during the release time (short solid black line) is denoted by $T(0d)$. The errors are given by caps at the edges of each bar and includes computation errors (shown in **figure 16.**), errors of ERA5 reanalysis data and variations of $T(0d)$ during each PNW event peak.

Changes of θ_e contributes to the particles' mean temperature $\Delta T_{\Delta\theta_e}$ increase was $9.9 \pm 2.5\,K$ within the last five days before these events, whereas $\Delta T_{\Delta\theta_e}$ ranged from $2.5 \pm 0.6\,K$ during event # 1 to $5.0 \pm 1.3\,K$ during events with $\Delta\theta_{net} < 4K$ (figure 21b). The larger extent of diabatic heating due to θ_e during events with $\Delta\theta_{net} > 4K$ can be explained by a longer period, in which the air mass remained at a lower altitude (figure 22a). Consequently, the air parcels did not cool by a rate of $1\,K$ per day as like those related to events with $\Delta\theta_{net} < 4K$. During event # 13, # 20, # 26, # 30 and # 32, the particles' median of potential temperature decreases by only about $1 - 2\,K$ from backward day 10 to 5 and increases further on (figure 21b). Thus, air parcels that arrived at these five events descended and radiative cooled not as much as air mass of other events with $\Delta\theta_{net} < 4K$. Notwithstanding, the fundamental driving processes like subsidence during events with $\Delta\theta_{net} > 4K$ were present as well, but not to such a great extent like other PNW events.

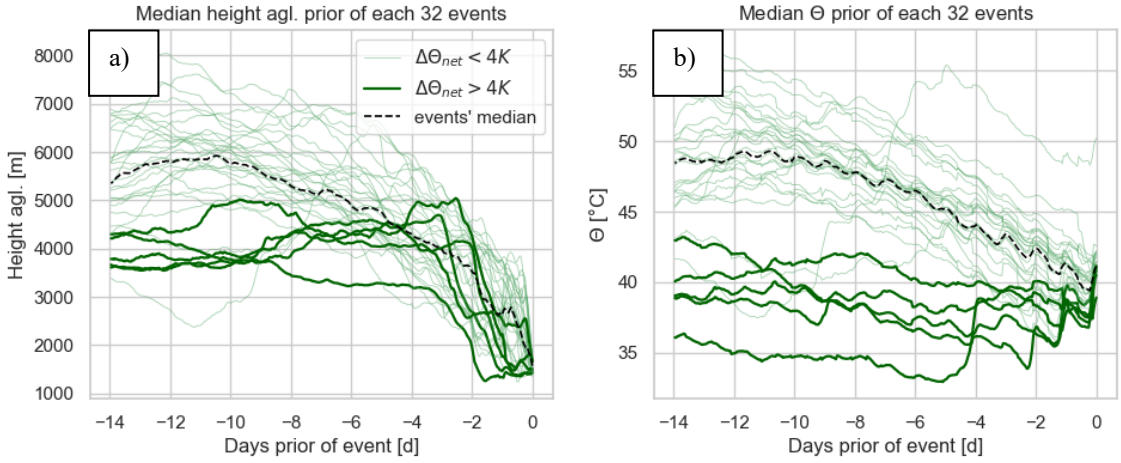

Figure 22. The temporal evolution of trajectories' median height and potential temperature before each PNW event. All bold solid dark green lines mark events with $\Delta\theta_{net} > 4K$ and all thin solid green lines are related to $\Delta\theta_{net} < 4K$ events. The black dashed line represents the events' median.

5.8 Adiabatic processes during PNW heat events

In this subsection, I evaluate the extent of adiabatic processes during the preceding 10 and 5 days of the PNW heat events. The particles' median of temperature increases by about $35\,K$ from backward day 5 to 0 during event # 1 (figure 18b)

and starts to descend from a higher altitude (figure 18a), whereas the particles' median temperatures increase by about $20\ K$ during the same period prior to the other PNW events. Furthermore, the particles' median pressures generally increase before each PNW event (figure 23b), but with two main differences. First, the air mass started to descent 5 days prior to the PNW June 2021 event peak, whereas the particles' starting time of descent was about 10 days prior to the other PNW heat events. Second, the total compression work was at a greater extent within five days before the PNW June 2021 event peak. The events' median pressure increases by about $120 - 130\ hPa$ while the particles' median pressure increases twice as much during the PNW June 2021 event within the last five days before arrival (figure 23b).

According to the Lagrangian energy equation, the pressure increase contributed to the particles' mean temperature by $46.5 \pm 2.3\ K$ during event # 1, by $26.4 \pm 4\ K$ during events with $\Delta\theta_{net} > 4K$ and by $32.8 \pm 5\ K$ during events with $\Delta\theta_{net} < 4K$ (figure 21b) within 5 days preceding to the respective events' peak. The results of $\Delta T_{\Delta p}$ confirms that the contribution of pressure increase to the particles' mean temperature are considerably greater ($15 - 20\ K$) during the PNW June 2021 heatwave. The particles' mean pressure increase within the last 5 days before the PNW June 2021 event is even greater than within the last 10 days before other PNW events.

Any meteorological conditions that favor descent and the conversion of potential temperature into sensible heat are indicated by the relative vorticity and the planetary boundary layer height, in which air mixes within an hour. To resolve large-scale circulation the particles' median of 24-hourly averaged relative vorticity before each of the respective PNW events is depicted in figure 23a. According to their values, the relative vorticity regarding to the PNW June 2021 event was less (up to $-5 \cdot 10^{-5}\ 1/s$) than those during previous events (up to $-2 \cdot 10^{-5}\ 1/s$). Furthermore, the particles' median of relative vorticity persists below $-2 \cdot 10^{-5}\ 1/s$ for a longer time (4 days) compared to previous events (1 day). Thus, the air parcels' descent rate was greater during the PNW June 2021 event than during previous PNW events within the preceding 5 days, especially from backward day 3 to 1, when the particles' median relative vorticity of event # 1 was the lowest.

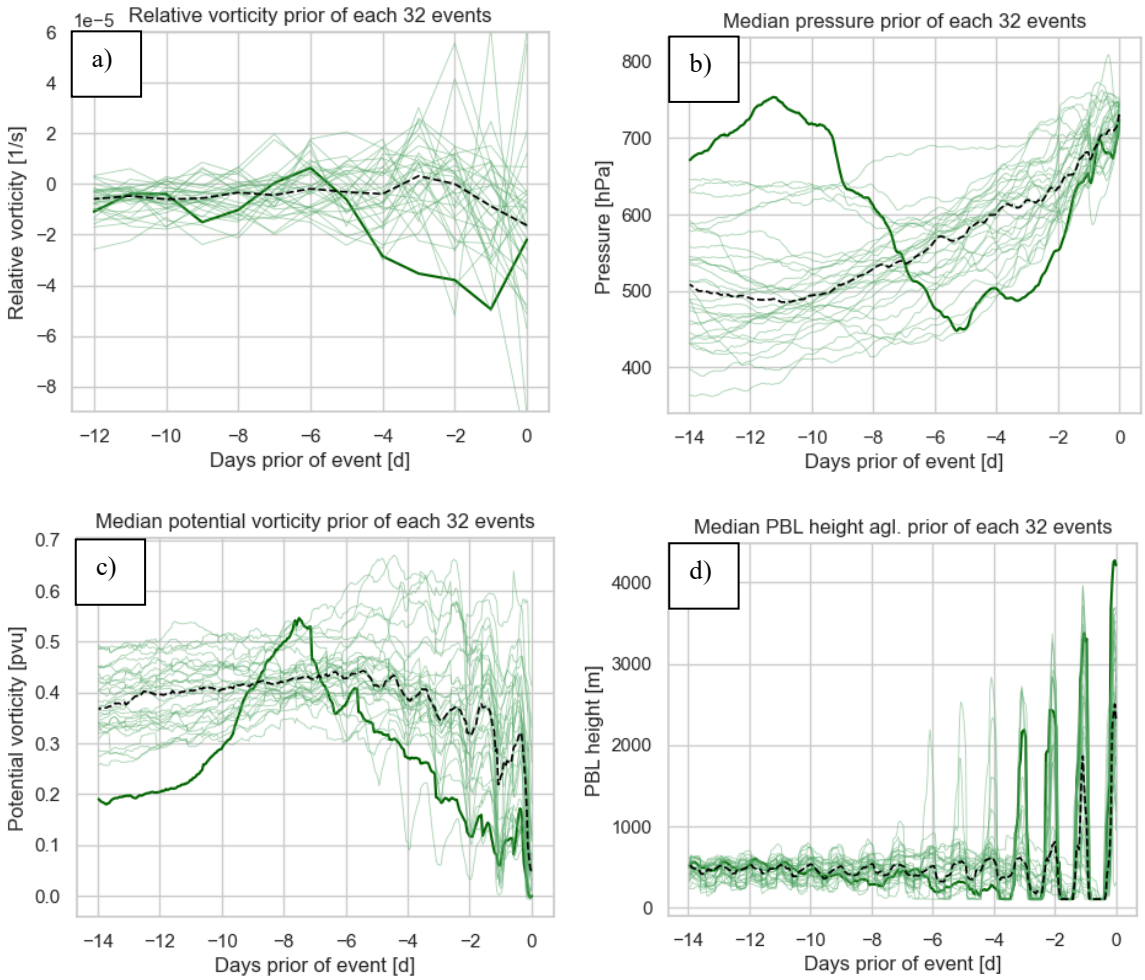

Figure 23. The temporal evolution of trajectories' median relative vorticity **(a)**, pressure **(b)**, potential vorticity **(c)** and the planetary boundary layer height **(d)** during all considered PNW events. The PNW June 2021 event is shown by a bold solid green line. The black dashed line on each panel represents the median of all identified PNW events. Each release date is during the respective peak of the PNW event.

Moreover, any differences in soil-moisture-temperature conditions are visible as differences in changes of specific moisture, which would increase to a less extent along trajectories over dry soils. During the 5 preceding days before the respective event's peak the increase in specific moisture decreased the particles' mean temperature by $-3.1 \pm 0.5\,K$ during event # 1, by $-4.7 \pm 0.7\,K$ during events with $\Delta\theta_{net} > 4K$ and by $-6.6 \pm 0.7\,K$ during events with $\Delta\theta_{net} < 4K$ (figure 21b). These results demonstrate that evaporative diabatic cooling of air parcels relating to the PNW June 2021 event was about $3.5\,K$ less than within air mass regarding to previous PNW heat events with $\Delta\theta_{net} < 4K$. Consequently, more energy was

available during event # 1 for partitioning surface fluxes towards sensible heat. Any partition of surface fluxes towards sensible heat leads to a faster increase in near surface temperatures and further enhances the lift of air parcels towards the boundary layer top. The more often air lifts off the surface, the higher the boundary layer finally grows during daytime and intense insolation (Baklanov, 2007). This contributed to the development of a higher boundary layer top and thus better conditions for air mass to descent from a higher altitude.

The mixing boundary layer height was about $4{,}200\,m$ on June 30, 2021, about $500\,m$ higher than the second highest of all 32 considered events (figure 23d). Assuming a dry adiabatic temperature lapse rate, the near surface temperatures potentially increased by up to 5 K within a 500 m higher boundary layer height on June 30, 2021. The positive soil-moisture-temperature feedback occurred because of a negative anomaly of skin reservoir content (figure 5a), moisture that is available for evaporation (Seneviratne et al., 2010). The summery (JJA) soil moisture decreases during climate change, especially in midlatitudes. Thus, heatwaves potentially occur more frequently, as climate models demonstrate (Seneviratne, 2006). Additionally, the growth of the planetary boundary layer could be supported by the extraordinary low relative humidity over the entire troposphere as well as over the entire affected area over the Pacific Northwest (figure 4 and figure 5b).

As a conclusion, the preceding latent heat release and its support to the persistence and intensity of atmospheric blockings acted like superpositions. Additionally, dry soil contributed to adiabatic heating as well. This situation underlies the remarkable difference in the onset of the PNW June 2021 heat event and the entirely different driving processes along the air parcels, which arrived Lytton on June 30, 2021. As the results (figure 18a) depict, the potential temperature ranged from about $39°C$ to $43°C$ during all previous PNW events' peak, whereas the value of it was about $50°C$ over Lytton on June 30, 2021. The closer an air parcel descent towards the surface during adiabatic heating processes, the closer the air parcel's temperature approaches to the value of potential temperature. Since adiabatic heating occurred during all events, the mentioned deviation of θ by at least $7\,K$ during the PNW June 2021 event explains why previous all-time 2-m temperature records have been broken by $6\,K$ or more on June 30, 2021.

6 Discussion

Some aspects of the evaluations applied in this master thesis and their caveats are discussed in this section. It includes a comparison of results with previous studies, sea surface anomalies during the PNW heat events and computation errors, which arise by applying the Lagrangian energy equation.

6.1 Caveats

Most of the Lagrangian results are depicted as particles' median and percentiles to obtain quantifiable portions, since the quantities are not normally distributed using a dispersion model. Furthermore, the comparison with other PNW events includes only the trajectories' median quantities, but not other percentiles. Consequently, any temporal evolutions of the outermost percentiles along trajectories during previous PNW events remain unrevealed. In addition, figure 16 contains only the particles' median latitude and longitudes, but not the outermost particles' contour lines in which the air mass of all PNW events are located because a hundred times more particles would be required to obtain a lucid chart with smooth lines. However, significant differences in the results about the origin and driving processes during the PNW heat events are unlikely because the main differences are clearly visible by using only the particles' median.

6.2 Comparison of results with previous studies

The differences between the results in this master thesis and in other previously published studies are discussed in this subsection. In general, the origin, the preceding latent heat release and the adiabatic heating during the PNW June 2021 event have been mentioned in other studies (Qian et al., 2022; Schumacher, Hauser & Seneviratne, 2022; Oertel et al., 2023; Röthlisberger & Papritz, 2023). Furthermore, some of these studies (e.g., Schumacher, Hauser & Seneviratne, 2022; Röthlisberger & Papritz, 2023) confirmed anomalous circulation patterns and significant higher planetary boundary layers during the PNW June 2021 event. The stated temperature deviations of $3.5\ K$ by a less moisture increase agrees with the

large-scale temperature anomalies of $3\,K$ risen by positive soil-moisture-temperature (Bartusek et al., 2022; Schumacher, Hauser & Seneviratne, 2022). The temperature deviation of $5\,K$ by a higher planetary boundary layer over Lytton agrees with the mentioned local temperature anomalies of $5\,K$, as discussed in a recent study about the PNW June 2021 event (Schumacher, Hauser & Seneviratne, 2022).

Notwithstanding, some other meteorological conditions, which could be related to the PNW June 2021 event, have not been fully evaluated by the mentioned studies. Firstly, any influence by typhoon Champi is excluded in this master thesis, whereas the role of a tropical storm before previous PNW heat events is not examined in other studies about the PNW June 2021 event (Bartusek et al., 2022; Lin, Mo & Vitart, 2022; Neal, Huang & Nakamura, 2022; Qian et al., 2022; Schumacher, Hauser & Seneviratne, 2022; Oertel et al., 2023; Röthlisberger & Papritz, 2023). However, it is not completely excluded that Champi affected other regions in the western Canadian Provinces and United States, since I only have released particles from a comparatively small area over Lytton.

Secondly, the source regions of air mass during the PNW events have not been compared together in a way like in figure 16, in which the climatology of θ_e in 500 hPa height over the North Pacific is compared with the origin of the PNW heat events' air parcels. Nevertheless, the subtropical origin from the western North Pacific is mentioned in studies about the onset of the PNW June 2021 event (Bartusek et al., 2022; Qian et al., 2022; Lin, Mo & Vitart, 2022; Schumacher, Hauser & Seneviratne, 2022; Oertel et al., 2023; Röthlisberger & Papritz, 2023). Finally, any connections between sea surface temperature anomalies and extreme PNW heat events, which have hardly been investigated, are evaluated in the next subsection.

6.3 Previous PNW events and their relation to ENSO and PDO

In this section all previous PNW events that I identified by applying the methods described in this thesis are listed in table 1 and discussed in this subsection. As the results illustrate, the approximately uniform distribution of the 32 most extreme

heat events from 1960 to 2021 is a result of detrending the daily maximum 2-m temperatures. The duration of each heat event ranges from 2 days to 7 days, except of event # 32 that persisted for 9 days in July 2009. Furthermore, the El Niño Southern Oscillation (ENSO) and the Pacific Decadal Oscillation (PDO, ERSST v5) indices during the respective month of the event are given in the fourth and fifth column in table 1. In general, the PDO phases have negative values during 25 out of the 32 (almost $80\ \%$) most extreme events, and the 7 positive values are mostly small. The climatological indices are utilized to evaluate their connections to the event's ranking or duration.

The Niño 3.4 index is calculated by averaging the monthly anomalies of sea surface over the eastern tropical Pacific from latitude 5°S to 5°N and longitude 170°W to 120°W. The variability of ENSO affects the anomalies of temperature and precipitation over many parts of the globe (Hao, Singh & Zhang, 2018). For instance, the amount of precipitation correlates not only over Australia (figure 2 in Hao, Singh & Zhang, 2018), but also precipitation events occur more frequently over some regions around China 6 month after a warm phase of ENSO (Li et al., 2011). Furthermore, a significant correlation between a warm phase of ENSO and high temperatures along the western coast of North America has been found (Hao, Singh & Zhang, 2018). Since, the air parcels of event # 1 arrived from the subtropical Pacific southwest of China to the Pacific Northwest, I expected a warm phase of ENSO. Nevertheless, the PNW June 2021 event occurred during a La Niña event, as the Niño 3.4 indices in 2021 indicates. Moreover, the given Niño 3.4 index varies and correlates neither with the rank nor with the duration of the 32 most extreme heat events over the Pacific Northwest within the time period from 1960 to 2021. The reason for this could be the different time scales of positive temperature anomalies defined here and in a study about correlations between ENSO and positive temperature anomalies (Hao, Singh & Zhang, 2018). Here, I used daily maximum temperatures that are higher than the 99^{th} percentile between 1960 and 2021, whereas the mentioned study (Hao, Singh & Zhang, 2018) considered monthly temperature data from 1951 to 2016, which are higher than the 80^{th} percentile.

Table 1. The 32 most extreme heat events between 1960 and 2021 (detrended data). The rank of each event is numbered in the first column. The given dates in the second column denote the peak day when the highest daily 2-m temperature during each heat wave was recorded. The duration of each heatwave is given in the third column. Two different monthly climatological indices (Niño 3.4, PDO) are noted in the last two columns. The bold entries in the last column highlight noticeable differences in the PDOs (the two highest values were in 2021).

Extreme PNW heat events over a 0.1° x 0.1° grid cell over Lytton.				
Ranking [1]	Date (YYYY-MM-DD)	Duration [2]	Niño 3.4 [3]	PDO [4]
1	2021-06-30	6 days	-1.00/-0.28	**-1.81**
2	1961-08-05	3 days	-0.35/-0.15	-0.87
3	1960-07-30	4 days	-0.46/-0.41	-0.42
4	1965-08-01	4 days	-0.34/1.12	0.32
5	2006-07-23	4 days	-0.67/0.01	0.39
6	1971-08-01	7 days	-1.36/-1.1	-0.32
7	1981-08-11	7 days	0.64/-0.53	-0.05
8	1994-07-25	6 days	0.06/0.24	-0.91
9	1979-07-20	4 days	-0.22/-0.47	0.30
10	1972-08-08	4 days	-0.19/1.09	-0.11
11	2021-07-31	2 days	-1.00/-0.39	**-1.91**
12	1967-08-31	3 days	-0.78/-0.42	**-1.55**
13	1998-07-27	4 days	2.03/-0.99	-1.16
14	1977-08-18	2 days	0.19/-0.01	-0.09
15	1971-08-11	6 days	-1.36/-1.1	-0.32
16	2021-08-14	2 days	-0.80/-0.53	-0.94
17	2015-06-28	3 days	0.51/1.18	0.82
18	2014-07-14	6 days	2.26/-0.06	0.25
19	1996-08-27	4 days	-0.61/-0.22	-0.66
20	2017-08-04	2 days	0.03/-0.16	-0.62
21	1986-08-28	3 days	-0.42/0.32	-0.19
22	1967-08-17	6 days	-0.78/-0.42	**-1.55**
23	1978-08-09	2 days	-0.20/-0.79	-0.91
24	1984-07-26	2 days	-0.19/-0.5	-0.35
25	1994-08-03	2 days	0.11/0.53	-0.88
26	1994-07-21	6 days	0.06/0.24	-0.91
27	1990-07-12	2 days	0.21/0.09	-0.31
28	2004-08-15	5 days	0.12/0.76	0.24
29	2018-08-10	4 days	-0.80/0.09	-0.24
30	1970-07-16	2 days	0.20/-1.08	-0.92
31	1985-07-30	3 days	-0.72/-0.74	0.52
32	2009-07-29	9 days	-0.79/0.48	-0.71

[1] Rank according to detrended daily maximum 2-m temperatures.
[2] Consecutive days with daily maximum 2-m temperatures above the 99th percentile.
[3] Monthly values are provided by the NOAA/CPC. The slash separates the Niño 3.4 values 6 months before and in the month of the PNW event.
[4] Provided by the NOAA's NCEI. Values are given for the month of event.

The PDO indices are usually obtained from EOF analysis over the northern Pacific (20°N – 70°N & 120°E – 120°W) of monthly averaged Extended Reconstructed Sea Surface Temperature Version 5 (ERSST v5) (Mantua et al., 1997; Huang et al., 2017), which are available on the NOAA's National Centers for Environmental Information (NCEI). A positive (negative) PDO is associated with negative (positive) anomalies of monthly SST in the interior North Pacific and positive (negative) anomalies of monthly SST along the Pacific Coast of North America (Mantua & Hare, 2002). Furthermore, positive (negative) anomalies of precipitation amount fall from the tropical Indian Ocean to the western subtropical Pacific during a cold (warm) PDO phase (Krishnamurthy & Krishnamurthy 2014).

As mentioned before, the PDO was negative during most of other PNW events and ranges from -1.91 to 0.82. The air parcels related to the PNW heat events originated from the interior of the North Pacific (figure 16) where positive anomalies of SST occur during a negative PDO phase. This could have contributed to the development of extreme near surface temperatures in the Pacific Northwest during these events. In addition, positive precipitation anomalies occurred over the western subtropical Pacific in early summer 2021 (Qian et al., 2022; Lin, Mo & Vitart, 2022) when PDO values during the 32 most extreme PNW heat events were the lowest (-1.81 in June 2021 and -1.91 in July 2021). Nevertheless, to verify or exclude any correlation between PDO values and the intensity of heatwaves over the PNW, further research by using more data is required.

6.4 Computation Error

It should be mentioned that any additional computation raises by applying the thermodynamic energy equation to the FLEXPART output data. In general, the particles' mean ratio of ΔT_{EE} and ΔT_{FP}, given in equation (16), increases in time and ranges from 0.96 to 1.12 (figure 24). Larger errors arise when air parcels jump into the boundary layer, in which all quantities like temperature and pressure change quickly. Since a larger portion of air mass is expected to enter the boundary layer towards the release date, any increase of the particles' median ratio of ΔT_{EE} and ΔT_{FP} is expected as well, which is in accordance to figure 24. In this evaluation the particles' mean ratio is only relevant at backward day 5 and 10, thus, the

computation errors within the considered time periods are less. In comparison to the FLEXPART output data the particles' mean total temperature change (red bars in figure 21) is underestimated by up to 4 % on backward day 10, whereas it is overestimated by up to 4 % on backward day 5. The errors are also considered in the calculated adiabatic and diabatic changes, which are depicted in figure 21 as bars.

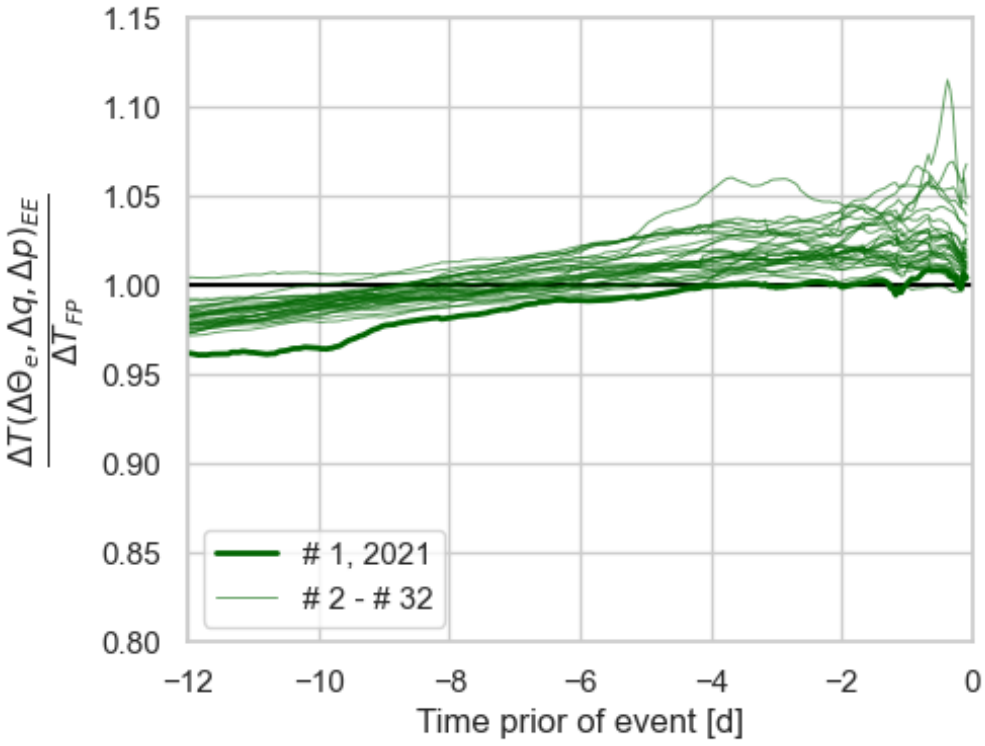

Figure 24. Equation (16), the trajectories' mean computation errors (green solid lines) that arise by applying the energy equation. The PNW June 2021 event is shown by a bold solid green line. By calculating the discrete differences, the start time, t_0, is fixed while the backward time, t, is variable and shown as a dependence along the x-axis. The errors are smallest when the ratio is 1 (black solid line).

7 Conclusion

In conclusion, the Lagrangian dispersion model FLEXPART revealed the most decisive driving processes during the PNW June 2021 heat event. First, a large portion of air mass originated from the subtropical western North Pacific where the air parcels took up large amounts of moisture. In the further course the air mass related to the PNW June 2021 event ascended and were heated diabatically by latent heat release along the Meiyu-Baiu-Front in the western Pacific and a warm conveyor belt in the northeastern Pacific preceding the subsidence. Furthermore, the latent heat release favored the onset of an intense persistent atmospheric blocking further downstream during the PNW June 2021 event. In addition, extraordinary low soil moisture contributed to the development of an about $500\,m$ higher planetary boundary layer, in which daily maximum near surface temperatures are potentially able to increase by about $5\,K$. Consequently, the air mass descended and adiabatically heated to a greater extent because of negative relative vorticities and a higher boundary layer prior to and during the event peak on June 30, 2021. However, the extreme near surface temperatures caused by adiabatic heating would not have occurred without the preceding latent heat release, which increased the potential temperature to about $50\,°C$ during the PNW June 2021 event peak.

The FLEXPART model also revealed the origin and driving processes during previous PNW heat events, which have been identified by a percentile-based method to detrended ERA5 reanalysis data. In contrast to the PNW June 2021 event, the air mass associated to previous PNW events originated from farther northern and eastern regions in the interior North Pacific where lower climatological values of θ_e dominate. In addition, most of the air mass associated with previous PNW events started to descend from the upper troposphere without any previous latent heat release and thus arrived at a considerably less potential temperature between $38\,°C$ and $43\,°C$ to the event peak. Moreover, the energy transport via atmospheric rivers like a warm conveyor belt could only have taken place during the PNW June 2021 event, otherwise a large portion air parcels would also have started from low altitudes before other PNW events.

As a final remark, the results in this master thesis confirm how entirely different the source region and subsequent main driving processes during the unprecedented “record-smashing” heatwave over the Pacific Northwest in late June 2021 were. Any relation to climate change and the PNW June 2021 event is not evaluated in this master thesis, but further research is required.

8 References

Baklanov, A., Atmospheric boundary layers: nature, theory, and application to environmental modelling and security. Springer. (2007).

Bartusek, S., Kornhuber, K. & Ting, M., North American heatwave amplified by climate change-driven nonlinear interactions. Nat. Clim. Chang. 12, 1143–1150 (2022). https://doi.org/10.1038/s41558-022-01520-4

Bieli, M., Pfahl, S., & Wernli, H. A Lagrangian investigation of hot and cold temperature extremes in Europe. Quarterly Journal of the Royal Meteorological Society, 141(686), 98–108. (2015): https://doi.org/10.1002/qj.2339

Bieli, M., Camargo, S. J., Sobel, A. H., Evans, J. L., & Hall, T. A Global Climatology of Extratropical Transition. Part I. Journal of Climate, 32(12), 3557–3582. (2019): https://doi.org/10.1175/JCLI-D-17-0518.1

Binder, H., Boettcher, M., Grams, C. M., Joos, H., Pfahl, S., & Wernli, H. Exceptional air mass transport and dynamical drivers of an extreme wintertime Arctic warm event. Geophysical ResearchLetters, 44, 12,028–12,036. (2017): https://doi.org/10.1002/2017GL075841

Bolton, D.: The computation of equivalent potential temperature. Mon. Wea. Rev., 108, 1046-1053, 1980, doi:10.1175/1520-0493(1980)108%3C1046:TCOEPT%3E2.0.CO;2.

Cassiani, M., Stohl, A., Olivié, D., Seland, Ø., Bethke, I., Pisso, I., and Iversen, T.: The offline Lagrangian particle model FLEXPART–NorESM/CAM (v1): model description and comparisons with the online NorESM transport scheme and with the reference FLEXPART model, Geosci. Model Dev., 9, 4029–4048, (2016): https://doi.org/10.5194/gmd-9-4029-2016

Chernykh, & Eskridge, R. E. Determination of Cloud Amount and Level from Radiosonde Soundings. Journal of Applied Meteorology (1988), 35(8), 1362–1369. (1996) https://doi.org/10.1175/1520-0450(1996)035<1362:docaal>2.0.co;2

Copernicus Climate Change Service, Climate Data Store: ERA5 hourly data on single levels from 1940 to present. Copernicus Climate Change Service (C3S) Climate Data Store (CDS), (2023), DOI: 10.24381/cds.adbb2d47 (Accessed on 20-02-2023)

Cornwall, M., Europe's deadly foods leave scientists stunned. https:// www.sciencemag.org/news/2021/07/europe-s-deadly-floodsleave-scientists-stunned (2021) (Retrieved 22 July 2021)

Davies-Jones, R.: On Formulas for Equivalent Potential Temperature. Mon. Wea. Rev., 137, 3137-3148, (2009) doi: 10.1175/2009mwr2774.1.

Döös, K., Jönsson, B., & Kjellsson, J. Evaluation of oceanic and atmospheric trajectory schemes in the TRACMASS trajectory model v6.0. Geoscientific Model Development, 10(4), 1733–1749. (2017) https://doi.org/10.5194/gmd-10-1733-2017

Eckhardt, S., Stohl, A., Wernli, H., James, P., Forster, C., & Spichtinger, N. A 15-Year Climatology of Warm Conveyor Belts. Journal of Climate, 17(1), 218–237., (2004): https://doi.org/10.1175/1520-0442(2004)017<0218:AYCOWC>2.0.CO;2

Hersbach, H., Bell, B, Berrisford, P, et al. The ERA5 global reanalysis. Q J R Meteorol Soc. (2020); 146: 1999– 2049. https://doi.org/10.1002/qj.3803

Eckhardt, S., A. Stohl, H. Wernli, P. James, C. Forster, and N. Spichtinger: A 15-year climatology of warm conveyor belts. J. Climate 17, 218-237. (2004)

Ertel, H. Ein neuer hydrodynamischer Erhaltungssatz. Naturwissenschaften 30, 543–544 (1942). https://doi.org/10.1007/BF01475602

Hao, F., Singh, V. P., & Zhang, X. Quantifying the relationship between compound dry and hot events and El Niño–southern Oscillation (ENSO) at the global scale. Journal of Hydrology (Amsterdam), 567, 332–338. (2018) https://doi.org/10.1016/j.jhydrol.2018.10.022

Holton, J.R. (2004) An Introduction to Dynamic Meteorology. Elsevier Academic Press, San Diego.

Hoskins, B. J., McIntyre, M. E., and Robertson, A. W.: On the use and significance of isentropic potential vorticity maps, Q. J. Roy. Meteor. Soc., 111, 877–946, 1985.

Hoskins, B., A potential vorticity view of synoptic development. Met. Apps, 4: 325-334. (1997): https://doi.org/10.1017/S1350482797000716

Huang, W., Thorne, P., Banzon, V. F., Boyer, T., Chepurin, G., Lawrimore, J. H., Menne, M. J., Smith, T. M., Vose, R. S., & Zhang, H.-M. Extended Reconstructed Sea Surface Temperature, Version 5 (ERSSTv5). Journal of Climate, 30(20), 8179–8205. (2017) https://doi.org/10.1175/JCLI-D-16-0836.1

Huang, W., Boyin & Liu, Chunying & Banzon, Viva & Freeman, J. & Graham, Garrett & Hankins, Bill & Smith, Tom & Zhang, Huai-Min. Improvements of the Daily Optimum Interpolation Sea Surface Temperature (DOISST) Version 2.1. Journal of Climate. 34. 1-47. (2020): 10.1175/JCLI-D-20-0166.1.

Krishnamurthy, & Krishnamurthy, V. Influence of PDO on South Asian summer monsoon and monsoon–ENSO relation. Climate Dynamics, 42(9-10), (2014): 2397–2410. https://doi.org/10.1007/s00382-013-1856-z

Kornhuber, K., Coumou, D., Vogel, E., Lesk, C., Donges, J. F., Lehmann, J., & Horton, R. M. Amplified Rossby waves enhance the risk of concurrent heatwaves in major breadbasket regions. Nature Climate Change, 10(1), 48–53. (2020): https://doi.org/10.1038/s41558-019-0637-z

Kunz, L., Konopka, P., Müller, R., & Pan, L. Dynamical tropopause based on isentropic potential vorticity gradients. Journal of Geophysical Research, 116(D1), n/a–n/a. (2011) https://doi.org/10.1029/2010JD014343

Li, W., P. Zhai, and J. Cai: Research on the relationship of ENSO and the frequency of extreme precipitation events in China. Adv. Clim. Change Res., 2(2), (2011) doi: 10.3724/SP.J.1248.2011.00101.

Lin., Y., Mesoscale Dynamics. Cambridge University Press. (2007) https://doi.org/10.1017/CBO9780511619649

Liu, S., and X.-Z. Liang, Observed diurnal cycle climatology of planetary boundary layer height, J. Clim., 22(21), 5790–5809, (2010): doi:10.1175/2010JCLI3552.1.

Mantua, N.J., S. R. Hare, Y. Zhang, J. M. Wallace, and R. C. Francis: A Pacific Interdecadal Climate Ooscillation with Impacts on Salmon Production. Bull. Amer. Meteor. Soc., 78, 1069-1079. (1997)

Mantua, & Hare, S. R. The Pacific Decadal Oscillation. Journal of Oceanography, 58(1), 35–44. (2002) https://doi.org/10.1023/A:1015820616384

Muñoz-Sabater, J.: ERA5-Land hourly data from 1950 to present. Copernicus Climate Change Service (C3S) Climate Data Store (CDS). (2019): DOI: 10.24381/cds.e2161bac (Accessed on 20-03-2023)

Oertel, A., Pickl, M., Quinting, J. F., Hauser, S., Wandel, J., Magnusson, L., et al. Everything hits at once: How remote rainfall matters for the prediction of

the 2021 North American heat wave. Geophysical Research Letters, 50, e2022GL100958. (2023). https://doi. org/10.1029/2022GL100958
Pfahl, Schwierz, C., Croci-Maspoli, M., Grams, C. M., & Wernli, H. Importance of latent heat release in ascending air streams for atmospheric blocking. Nature Geoscience, 8(8), 610–614. (2015) https://doi.org/10.1038/ngeo2487
Philip, S. Y., Kew, S. F., Van Oldenborgh, G. J., Anslow, F. S., Seneviratne, S. I., Vautard, R., Coumou, D., Ebi, K. L., Arrighi, J., Singh, R., Van Aalst, M., Pereira Marghidan, C., Wehner, M., Yang, W., Li, S., Schumacher, D. L., Hauser, M., Bonnet, R., Luu, L. N., … Otto, F. E. Rapid attribution analysis of the extraordinary heat wave on the Pacific coast of the US and Canada in June 2021. Earth System Dynamics, 13(4), 1689–1713. (2022) https://doi.org/10.5194/esd-13-1689-2022
Pisso, I., Sollum, E., Grythe, H., Kristiansen, N.I., Cassiani, M., Eckhardt, S., Arnold, D., Morton, D., Thompson, R.L., Groot Zwaaftink, C.D., Evangeliou, N., Sodemann, H., Haimberger, L., Henne, S., Brunner, D., Burkhart, J.F., Fouilloux, A., Brioude, J., Philipp, A., Seibert, P., and Stohl, A.: FLEXPART 10.4 (Version 10.4), Geosci. Model Dev. Discuss. Zenodo, (2019) https://doi.org/10.5281/zenodo.3542278, 2019.
Ramli, H. M. and Esler, J. G.: Quantitative evaluation of numerical integration schemes for Lagrangian particle dispersion models, Geosci. Model Dev., 9, 2441–2457, https://doi.org/10.5194/gmd-9-2441-2016, 2016.
Rastigejev, Y., Park, R., Brenner, M. P., and Jacob, D. J., Resolving intercontinental pollution plumes in global models of atmospheric transport, J. Geophys. Res., 115, D02302, (2010) doi:10.1029/2009JD012568.
Röthlisberger, M., Papritz, L. Quantifying the physical processes leading to atmospheric hot extremes at a global scale. Nat. Geosci. 16, 210–216 (2023). https://doi.org/10.1038/s41561-023-01126-1
Schumacher, D. L., Hauser, M., & Seneviratne, S. I. Drivers and mechanisms of the 2021 Pacific Northwest heatwave. Earth's Future, 10, (2022) e2022EF002967. https://doi. org/10.1029/2022EF002967
Seneviratne, S., Luethi, D., Litschi, M., & Schaer, C. Land-atmosphere coupling and climate change in Europe. Nature, 443(7108), 205–209. (2006) https://doi.org/10.1038/nature05095
Seneviratne, S., Corti, T., L. Davin, E., Hirschi, M., B. Jaeger, M., Lehner, I., Orlowsky, B., J. Teuling, A., Investigating soil moisture–climate interactions in a changing climate: A review, Earth-Science Reviews, Volume 99, Issues 3–4, Pages 125-161, ISSN 0012-8252, (2011) https://doi.org/10.1016/j.earscirev.2010.02.004.
Siebesma, A. P., Bony, S., Jakob, C., & Stevens, B. Clouds and Climate. Cambridge University Press. (2020) https://doi.org/10.1017/9781107447738
Sprenger, M. and Wernli, H.: The LAGRANTO Lagrangian analysis tool – version 2.0, Geosci. Model Dev., 8, 2569–2586, https://doi.org/10.5194/gmd-8-2569-2015, (2015).
Steinfeld, D. & Pfahl, S.: The role of latent heating in atmospheric blocking dynamics: a global climatology, Clim. Dynam., 53, 6159–6180, https://doi.org/10.1007/s00382-019-04919-6, (2019).
Steinfeld, D., Boettcher, M., Forbes, R., & Pfahl, S. The sensitivity of atmospheric blocking to upstream latent heating – numerical experiments. Weather and Climate Dynamics. (2020). https://doi.org/10.3929/ethz-b-000456732

Stohl, A., Forster, C., Eckhardt, S., Spichtinger, N., Huntrieser, H., Heland, J., Schlager, H., Wilhelm, S., Arnold, F., and Cooper, O.: A backward modeling study of intercontinental pollution transport using aircraft measurements, J. Geophys. Res., 108, 4370, doi:10.1029/2002JD002862, (2003).

Stohl, A., Forster, C., Frank, A., Seibert, P., and Wotawa, G.: Technical note: The Lagrangian particle dispersion model FLEXPART version 6.2, Atmos. Chem. Phys., 5, 2461–2474, https://doi.org/10.5194/acp-5-2461-2005, (2005).

Van Wagner, C. E.: Development and Structure of the Canadian Forest Fire Weather Index System, Technical Report 35, Canadian Forestry Service, Ottawa, ON, (1987)

9 Appendix

Abstract

During the extreme Pacific Northwest June 2021 heat wave previous all-time 2-m temperature records were broken by $5\ K$ or more. The highest 2-m temperature of $49.6°C$ on June 30 was measured in Lytton, a village in the Canadian province British-Columbia (50.2°N). To address the question why this event was so anomalous, I applied the Lagrangian dispersion model FLEXPART to obtain analysis data of 15-day backward trajectories and to trace meteorological parameters and physical quantities along them. This master thesis includes a case study of the PNW June 2021 event and an analysis of the 32 most extreme PNW heat events between 1960 and 2021. First, large portions of air mass associated with the PNW June 2021 event originated from subtropical regions in the western North Pacific and thus unusually far southern and western compared to previous PNW heat events. Secondly, the moisture uptake and subsequent latent heat release due to condensation along the Meiyu-Baiu-Front and a warm conveyor belt contributed decisively to the intensity of the PNW June 2021 event. Consequently, the potential temperature increased to about $50°C$ in Lytton on June 30, 2021, $7 - 11\ K$ above those values during previous most extreme heat events' peak over the Pacific Northwest. Moreover, the latent heat release, which occurred only before the PNW June 2021 event, contributed to the onset of an intense persistent atmospheric blocking over the Pacific Northwest. In addition, positive soil-moisture-temperature feedback was favored by low moisture conditions and led to the development of a higher boundary layer top on June 30, 2021. Therefore, adiabatic heating by descent and mixing occurred to a greater extent than during previous PNW heat events. Thus, to summarize, two superimposed main driving processes could be identified only during the June 2021 PNW event. This explains why the 2-m temperature maxima on June 30, 2021, over the Pacific Northwest deviated by $5\ K$ or more from previous 2-m temperature records.

Zusammenfassung

Während der extremen Hitzewelle im Pazifischen Nordwesten im Juni 2021 wurden frühere 2-m-Temperaturrekorde um $5\,K$ oder mehr gebrochen. Die höchste 2-m Temperatur von $49{,}6°C$ wurde am 30. Juni in Lytton, einem Dorf in der kanadischen Provinz British-Columbia (50,2°N), gemessen. Um der Frage nachzugehen, warum dieses Ereignis derart extrem war, habe ich das Lagrangesche Ausbreitungsmodell FLEXPART angewandt, um Analysedaten von 15-tägigen Rückwärtstrajektorien zu erhalten und um meteorologische Parameter und physikalische Größen entlang dieser zu verfolgen. Diese Masterarbeit beinhaltet eine Fallstudie des PNW-Hitzeereignisses vom Juni 2021 und eine Analyse der 32 extremsten PNW-Hitzeereignisse zwischen 1960 und 2021. Erstens stammen große Teile der Luftmassen, die mit dem PNW-Ereignis im Juni 2021 in Verbindung stehen, von subtropischen Regionen im westlichen Nordpazifik und damit ungewöhnlich weit südlich und westlich im Vergleich zu früheren Hitzeereignissen. Des Weiteren trug die Feuchteaufnahme und die anschließende Freisetzung latenter Wärme durch Kondensation entlang der Meiyu-Baiu-Front und eines Warm Conveyor Belts entscheidend zu der Intensität der PNW-Hitzewelle im Juni 2021 bei. Infolgedessen stieg die potenzielle Temperatur am 30. Juni 2021 in Lytton auf etwa $50\,°C$ und lag damit 7 bis $11\,K$ über den Werten der früheren extremsten PNW-Hitzewellen. Darüber hinaus begünstigte die latente Wärmefreisetzung, die nur vor der PNW-Hitzewelle im Juni 2021 auftrat, die Entstehung eines intensiven anhaltenden blockierenden Hochdruckgebietes über dem Pazifischen Nordwesten. Zusätzlich entwickelte sich aufgrund einer unterdurchschnittlichen Bodenfeuchte, die zu einer positiven Rückkopplung zwischen der Bodenfeuchte und der Temperatur führte, am 30. Juni 2021 eine höhere Grenzschicht. Infolgedessen war die adiabatische Erwärmung durch Senkung und Durchmischung während des PNW-Hitzeereignisses im Juni 2021 intensiver als während früherer PNW-Hitzewellen. Zusammenfassend lassen sich zwei primäre überlagernde Antriebsprozesse nur während des PNW-Ereignisses im Juni 2021 feststellen. Dies erklärt warum die 2-m Temperaturmaxima am 30.Juni 2021 über dem Pazifischen Nordwesten um $5\,K$ oder mehr von den bisherigen 2-m Temperaturrekorden abwichen.